A&A 569, A17 (2014)
DOI: 10.1051/0004-6361/201423851

Astronomy & Astrophysics

The *Gaia*-ESO Survey: Stellar content and elemental abundances in the massive cluster NGC 6705⋆,⋆⋆

T. Cantat-Gaudin[1,2], A. Vallenari[2], S. Zaggia[2], A. Bragaglia[3], R. Sordo[2], J. E. Drew[4], J. Eisloeffel[5], H. J. Farnhill[4], E. Gonzalez-Solares[6], R. Greimel[7], M. J. Irwin[6], A. Kupcu-Yoldas[6], C. Jordi[8], R. Blomme[9], L. Sampedro[10], M. T. Costado[10], E. Alfaro[10], R. Smiljanic[11,12], L. Magrini[13], P. Donati[3,14], E. D. Friel[15], H. Jacobson[16], U. Abbas[18], D. Hatzidimitriou[19], A. Spagna[18], A. Vecchiato[18], L. Balaguer-Nunez[8], C. Lardo[3], M. Tosi[3], E. Pancino[3], A. Klutsch[20], G. Tautvaisiene[17], A. Drazdauskas[17], E. Puzeras[17], F. Jiménez-Esteban[26], E. Maiorca[13], D. Geisler[24], I. San Roman[24], S. Villanova[24], G. Gilmore[21], S. Randich[13], T. Bensby[22], E. Flaccomio[23], A. Lanzafame[20], A. Recio-Blanco[25], F. Damiani[23], A. Hourihane[21], P. Jofré[21], P. de Laverny[25], T. Masseron[21], L. Morbidelli[13], L. Prisinzano[23], G. G. Sacco[13], L. Sbordone[27,28], and C. C. Worley[21]

(Affiliations can be found after the references)

Received 20 March 2014 / Accepted 26 June 2014

ABSTRACT

Context. Chemically inhomogeneous populations are observed in most globular clusters, but not in open clusters. Cluster mass seems to play a key role in the existence of multiple populations.

Aims. Studying the chemical homogeneity of the most massive open clusters is needed to better understand the mechanism of their formation and determine the mass limit under which clusters cannot host multiple populations. Here we studied NGC 6705, which is a young and massive open cluster located towards the inner region of the Milky Way. This cluster is located inside the solar circle. This makes it an important tracer of the inner disk abundance gradient.

Methods. This study makes use of *BVI* and *ri* photometry and comparisons with theoretical isochrones to derive the age of NGC 6705. We study the density profile of the cluster and the mass function to infer the cluster mass. Based on abundances of the chemical elements distributed in the first internal data release of the *Gaia*-ESO Survey, we study elemental ratios and the chemical homogeneity of the red clump stars. Radial velocities enable us to study the rotation and internal kinematics of the cluster.

Results. The estimated ages range from 250 to 316 Myr, depending on the adopted stellar model. Luminosity profiles and mass functions show strong signs of mass segregation. We derive the mass of the cluster from its luminosity function and from the kinematics, finding values between 3700 $M_{\odot}$ and 11 000 $M_{\odot}$. After selecting the cluster members from their radial velocities, we obtain a metallicity of [Fe/H] = 0.10 ± 0.06 based on 21 candidate members. Moreover, NGC 6705 shows no sign of the typical correlations or anti-correlations between Al, Mg, Si, and Na, which are expected in multiple populations. This is consistent with our cluster mass estimate, which is lower than the required mass limit proposed in the literature to develop multiple populations.

Key words. stars: abundances – open clusters and associations: general – open clusters and associations: individual: NGC 6705

1. Introduction

Once thought to be the best example of simple stellar populations (coeval, mono-metallic systems), the globular clusters (GCs) have been shown to instead be complex objects. In particular, evidence that they host distinct populations (possibly distinct generations) of stars has been mounting. Gratton et al. (2004, 2012) present reviews based on spectroscopy, while Piotto (2009) and Milone et al. (2012) can be consulted for results based on photometry.

While variations in iron content seem limited to very few cases, the most notable being ω Cen (e.g. Lee et al. 1999; Johnson & Pilachowski 2010) and M 22 (e.g. Marino et al. 2011), GC stars show large star-to-star variations in some light elements, such as C, N, O, Na, Mg, and Al. It has been known for a long time that there are variations in the CN and CH bands strengths with spreads and bimodal distributions (e.g. Kraft 1979, 1994, for reviews), and not all the variations can be attributed to internal processes like mixing. Na and O have been extensively studied as summarised in the review by Gratton et al. (2004) and Carretta et al. (2009a,b), which show an anti-correlation: in the same GC there are stars with "normal" O and Na (normal with respect to the cluster metallicity) and stars showing a (strong) depletion in O and an enhancement in Na. Most of the stars have a modified composition. A similar anti-correlation can be found between Mg and Al, but not in all clusters, and with lower depletions than in O (e.g. Carretta et al. 2009b; Marino et al. 2008). Most importantly, these star-to-star variations also occur in unevolved, main-sequence stars, as demonstrated first by Gratton et al. (2001) and Ramírez & Cohen (2002) and later confirmed on much larger samples (e.g. Lind et al. 2009; D'Orazi et al. 2010). These low-mass stars cannot have produced these variations, since their cores do not reach the high temperatures necessary for the relevant proton-capture

⋆ Based on the data obtained at ESO telescopes under programme 188.B-3002 (the public *Gaia*-ESO spectroscopic survey, PIs Gilmore and Randich) and on the archive data of the programme 083.D-0671.

⋆⋆ Full Table 2 is only available at the CDS via anonymous ftp to cdsarc.u-strasbg.fr (130.79.128.5) or via http://cdsarc.u-strasbg.fr/viz-bin/qcat?J/A+A/569/A17

reactions, and in any case, the stars lack the mixing mechanism needed to bring processed material to the surface. This implies that the chemical inhomogeneities were already present in the gas out of which these stars formed. This has led to the belief that GCs are made of at least two generations of stars, with the second generation formed from gas polluted by the material processed by the first. Exactly which kind of first-generation stars were the polluters is debated; the most promising candidates are intermediate-mass asymptotic giant branch stars (Ventura et al. 2001) and fast-rotating massive stars (Decressin et al. 2007), but refinements and comparisons to robust observational constraints are required.

The multiple population scenario for GCs requires that the cluster is massive enough to retain some of its primordial gas; indeed, existing models postulate that GCs were many times more massive at the time of their formation than they appear today (e.g. D'Ercole et al. 2008). Such models suffer from several drawkbacks. For instance, they do not explain the observed properties of the young massive clusters (Bastian & Silva-Villa 2013) or the abundance patterns of the halo stars (see e.g. Martell et al. 2011). Recently, a mechanism based on accretion on circumstellar discs, which does not require multiple generation of stars, has been presented by Bastian et al. (2013). This model does not require that clusters were initially extremely massive. In any case, the efficiency of the accretion process depends on the density and velocity dispersion of the cluster, which both scale with the cluster mass, suggesting that more massive clusters should exhibit broader chemical dishonomegeneities.

Carretta et al. (2010) combined the data on 18 GCs of the FLAMES survey (Carretta et al. 2009a) and literature studies to showe that all Galactic GCs for which Na and O abundances were available presented a Na-O anti correlation, i.e. multiple populations. The only possible exceptions were Terzan 7 and Palomar 12, two young and low-mass GCs belonging to the Sagittarius dwarf galaxy. It was suggested that this apparent universality of the Na-O anti correlation is a defining property of GCs, separating them from the other clusters where only a single population is present. Cluster mass seems to play a determinant role in this separation, and studies of low-mass GCs and massive and old open clusters (OCs) are needed to determine the mass threshold under which no multiple populations can be formed. This scenario needs, however, to be verified observationally, which motivated further studies in this "grey zone" between the two kind of clusters. Recent additions include the (i) GCs Rup 106 (Villanova et al. 2013), which shows no Na-O anti-correlation; (ii) and Terzan 8 (Carretta et al. 2013), in which the second generation, if present, represents a minority; and (iii) two of the most massive and oldest OCs, Berkeley 39 and NGC 6791. High-resolution spectroscopy in 30 stars of Berkeley 39 by Bragaglia et al. (2012) shows a single, homogeneous population. Geisler et al. (2012) have found signs of a bi-modal Na distribution in NGC 6791, which would make it the first known OC with multiple populations. This suggestion has not been confirmed by another study (Bragaglia et al. 2013, submitted) where no variations exceeding the errors were found in the same cluster. Further studies are called for to settle the issue.

The *Gaia*-ESO Survey (hereafter GES, Gilmore et al. 2012; Randich & Gilmore 2013) is a large, public spectroscopic survey using the high-resolution multi-object spectrograph FLAMES on the Very Large Telescope (ESO, Chile). It targets more than 10^5 stars, covering the bulge, thick and thin discs, and halo components, and a sample of about 100 open clusters (OCs) of all ages, metallicities, locations, and masses. The focus of the GES is to quantify the kinematical and chemical element abundance distributions in the different components of the Milky Way, thus providing a complement to the limited spectroscopic capabilities of the astrometric *Gaia* mission.

Here we focus on NGC 6705 (M 11, Mel 213, Cr 391, OCl 76), a massive and concentrated OC located in the first galactic quadrant (Messina et al. 2010; Santos et al. 2005) at the galactic coordinates ($l = 27.3$, $b = -2.8$). This cluster, one of the three intermediate-age clusters observed in the first GES internal data release, contains a total of several thousand solar masses (McNamara & Sanders 1977; Santos et al. 2005), which places it near the limit between the most massive OCs and the least massive GCs (Bragaglia et al. 2012). Since it is located towards the central parts of the Galaxy it is projected against a dense background, but its rich main sequence and populated red clump clearly stand out in a colour-magnitude diagram (CMD).

NGC 6705 is situated in a clear area and suffers from relatively little extinction for an object at such a low galactic latitude. Moreover, its position inside the solar circle makes it an important tracer of the inner disk gradient. In a companion paper, Magrini et al. (2014) compare the abundance patterns of the three intermediate-age OCs of the first GES data release (NGC 6705, Tr 20 and NGC 4815) for Fe, Si, Mg, Ca, and Ti. They show that each cluster has a unique pattern, in particular with a high value for [Mg/Fe] in NGC 6705. Moreover, the abundances of two of these clusters are consistent with their galactocentric radius, whereas the abundances of NGC 6705 are more compatible with a formation between 4 and 6 kpc from the Galactic centre despite its current galactocentric radius of 6.9 kpc. The present paper focuses on the determination of the structural parameters, age and chemical abundances of NGC 6705 using VPHAS+, ESO 2.2.m telescope WFI photometry, and spectroscopic data from the GES.

The photometric and spectroscopic data are presented in Sect. 2. The membership determination is given in Sect. 3. In Sect. 4 we derive the extintion map in the region surrounding the cluster. In Sect. 5 we study the luminosity profile and mass segregation of the cluster, and provide cluster mass estimates. In Sect. 6 we look at the rotation and kinematics in the cluster. In Sect. 7 we make use of isochrones to determine the distance and age of the cluster. Finally, the chemical abundances of Al, Mg, Si, and Na for NGC 6705 are presented in Sect. 8.

2. The data

2.1. WFI BVI photometry

The photometry used in this paper has been extracted from archival images in B, V and I taken on the 13 May 1999 with the Wide Field Imager at the MPG/ESO 2.2 m Telescope for the ESO Imaging Survey (ESO programme 163.O-0741(C), PI Renzini). The sample of images comprise for each band two long exposure time images (240 s each for a total of 480 s), in order to reach a photometric precision of 20% at $V \simeq 21$ mag, and single short (20 s) exposure carefully chosen not to saturate the brighter targets.

Data reduction has been performed using the ESO/Alambic software (Vandame 2002) especially designed for mosaic CCD cameras and providing fully astrometrically and photometrically calibrated images with special care to the so-called "illumination correction". The photometry was performed using the Daophot/Allstar software (Stetson 1987) wrapped in an automatic procedure that performed the PSF calculation and all the steps for extracting the final magnitudes. The PSF photometry from the short and long exposures for each single band have been

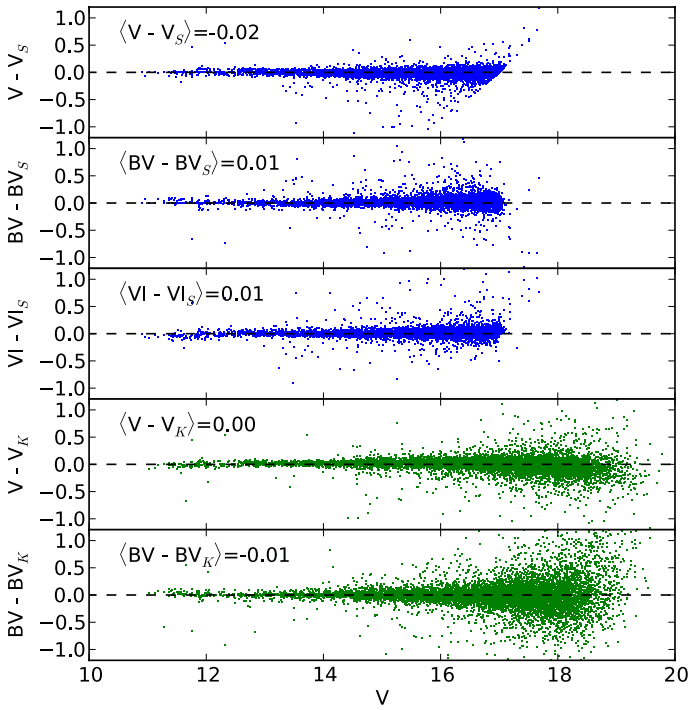

Fig. 1. *Upper three panels*: comparison of our photometry with that of Sung et al. (1999). *Lower two panels*: comparison with Koo et al. (2007). The labels indicate the residual zero point differences.

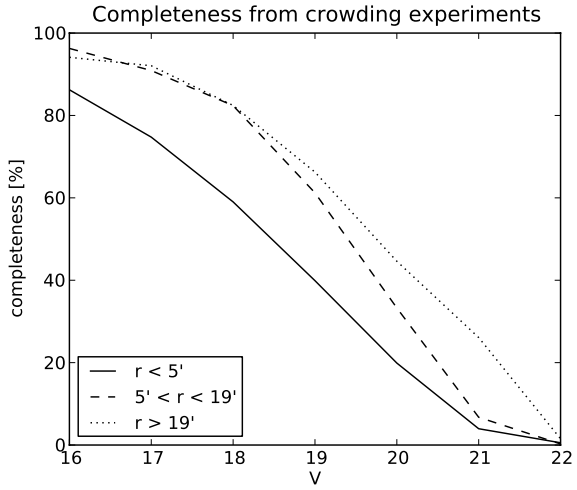

Fig. 2. Completeness of our photometry obtained from crowding experiments for different regions of the cluster.

combined in a single photometric dataset using the Daomaster program. The internal astrometric accuracy (both within the short/long exposures and in the different bands) turned out to be better than 0.05 arcsec, while the external comparison with the 2MASS catalogue gave a root mean square of ≃0.20 arcsec.

The observations consist in a single $33' \times 34'$ field centred on the cluster, completely covering the photometry of Sung et al. (1999). The geometry of the WFI imaging is shown in Fig. 9. We tied our instrumental WFI photometry to their photometric calibration, comparing the magnitudes of the common objects and calculating solutions for the zero point and colour term for each pass band. In the magnitude range $V < 14$ the dispersion is of the order of 0.05 mag, increasing to 0.1 for stars as faint as $V \sim 17$ (see the upper panels of Fig. 1). Unfortunately, the B-band filter of WFI is quite far from the Johnson B filter with a large colour term of ≃−0.33 mag. After applying the calibration, the B magnitudes present a residual second-order trend in colour that appears as a residual offset of −0.05 mag for the extreme blue and red stars. We decided not to apply any correction for this effect and instead used the photometry of Sung et al. (1999) for all objects with $V < 12$ and $(B - V) > 1$. For fainter stars, the photometries show good agreement, with a residual offset of ≃0.02 mag at $V = 14$, increasing to 0.1 mag at $V \simeq 17$. The comparison between our photometry and that of Sung et al. (1999) is shown in the upper three panels of Fig. 1.

Our data were also compared with the BV photometric data of Koo et al. (2007), acquired in a search for variable stars. The comparison (lower panels of Fig. 1) also shows good agreement with no systematics, with a dispersion of 0.08 for $V < 14$, increasing for fainter magnitudes.

Since the cluster is very dense, our photometry suffers from crowding effects, especially in the central parts. The completeness of the photometry was estimated as usual by randomly adding stars of magnitude V ranging from 16 to 22 and running the source detection step again, then counting how many of the added stars were recovered. This method allows to estimate the completeness for each magnitude bin in a given region of the cluster. The completeness is better than 50% up to magnitude $V \simeq 18$ in the central regions and $V \simeq 19.7$ in the less crowded outskirts (see Fig. 2).

The data contain a total of 123 037 stars. The BV CMD shows a very clear main sequence standing out of the background as can be seen in Fig. 3. Evolved stars are also visible with a red clump located around $(B-V, V) = (1.5, 12)$. The lower panels of Fig. 3 show that the main sequence can be easily followed down to $V = 16$ in the inner regions of the cluster, while the top right-hand panel shows that the signature of the cluster is not visible outside of 18′.

2.2. VPHAS+ *ri* photometry

The VPHAS+ observations used here are r- and i-band data from three fields (numbered 212, 213, and 237) that overlap near the sky position of NGC 6705. A general description of this public survey that continues to execute using the OmegaCAM instrument on the VLT Survey Telescope is provided by Drew et al. (2014). Each pointing captures a square degree at a time, with the centre of NGC 6705 falling within a couple of arcminutes of the southern edge of field 212, and towards the boundary with 237. The data were all obtained at a time of very good seeing (0.5 to 0.6 arcseconds) during the night of 7 July 2012 when the moon was relatively bright (FLI = 0.77). In r, the formal 10σ magnitude limit falls between 20.5 and 20.8 with a likely completeness limit of ∼19.5, while these limits are approximately 0.5−0.7 mag brighter in the i band. All magnitudes are specified in the Vega system.

The CMD of the inner 12′ is shown in Fig. 4. The data are used in Sect. 4 to derive the extinction map of the region surrounding the cluster. Owing to the very good seeing, stars brighter than $r \sim 12$ are partially saturated in both r and i bands, making the position of the main sequence turn-off point and red clump stars quite uncertain in the CMD.

2.3. GES spectroscopic data

The GES makes use of the GIRAFFE ($R \sim 20\,000$) and UVES ($R \sim 47\,000$) spectrographs of the VLT UT-2. The GES consortium is structured in several working groups (WGs). The

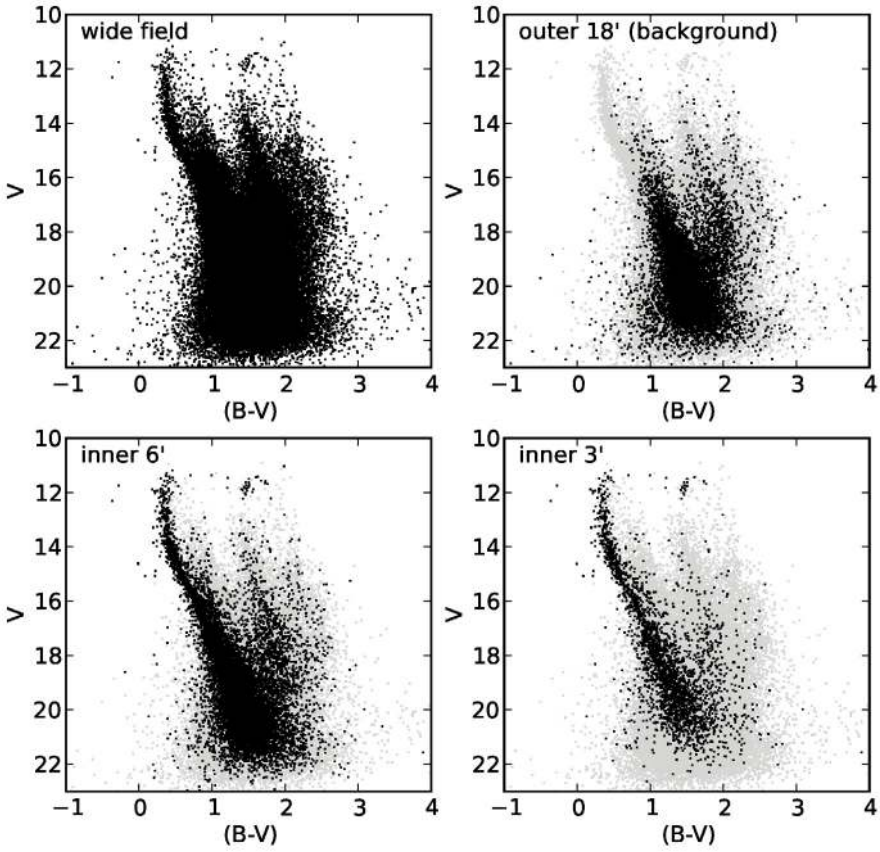

Fig. 3. *Top left*: *BV* CMD of all 123 037 in our sample. *Top right*: CMD of the outer 18′, which we consider as our background field. *Bottom left* and *bottom right*: CMD of the inner 6′ and 3′. In the last three panels, the grey points correspond to the wide-field CMD.

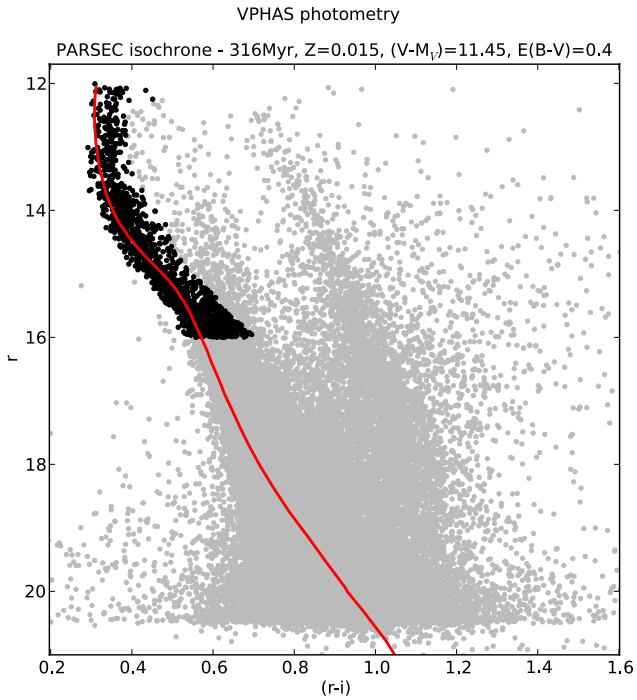

Fig. 4. VPHAS+ *ri* CMD of the central 12′ of the cluster. The spatial distribution of the selected stars (black points) is shown in Fig. 9. The solid line corresponds to the PARSEC isochrone of best parameters, shifted for distance modulus and extinction (see Sect. 7 for detail). Stars brighter than $r = 12$ suffer from saturation and are not shown here.

reduction of the GIRAFFE and UVES spectra by WG7 is described in Lewis et al. (in prep.) and Sacco et al. (2014), respectively. The analysis is performed independently by teams using different methods, but making use of the same model atmospheres (MARCS, Gustafsson et al. 2008) and the same line list (Heiter et al., in prep.). The results are then gathered and controlled to produce a homogenised set (for a comparison of the results obtained with different spectroscopic methods, see for instance Jofre et al. 2014). The analysis of the GIRAFFE data by WG10 is described in Recio-Blanco et al. (in prep.), and the analysis of UVES spectra by WG11 is described in Smiljanic et al. (in prep.).

Stellar parameters and elemental abundances for the stars observed during the first six months of the campaign were delivered to the members of the collaboration as an internal data release (internal data release 1, or GESviDR1Final) for the purpose of science verification and validation.

The target selection for NGC 6705 and the exposure times for the various setups are described in Bragaglia et al. (in prep.). For the GIRAFFE targets, potential members were selected on the basis of their optical and infrared photometry following the cluster main sequence, and the proper motions from the UCAC4 catalog (see Zacharias et al. 2012) were used in order to discard objects whose proper motions are more than five sigma from the cluster centroid. In total, 1028 main-sequence stars were observed with eight GIRAFFE setups. All the red giants located in the clump region in the inner 12′ were observed with the UVES setup 580 (25 targets). The number of targets observed with each GIRAFFE setup are summarised in Table 1. The coordinates, *B*, *V*, *J*, *H*, and *K* magnitudes, radial velocities and membership probabilities (see Sect. 3) are shown in Table 2.

The spatial distribution of the targets is shown in the top left-hand panel of Fig. 5, and the *BV* photometry of the targets is the WFI photometry presented in the present paper. The bottom left-hand panel of Fig. 5 shows the radial velocity (RV) distribution of all the GIRAFFE targets. From the GESviDR1Final data

Table 1. Summary of GES GIRAFFE observations.

Setup	Central λ [nm]	Spectral range [nm]	R	Nb stars	Median S/N
HR3	412.4	403.3–420.1	24 800	166	24
HR5A	447.1	434.0–458.7	18 470	166	25
HR6	465.6	453.8–475.9	20 350	166	21
HR9B	525.8	514.3–535.6	25 900	526	37
HR10	447.1	434.0–458.7	18 470	284	50
HR14A	651.5	630.8–670.1	17 740	166	44
HR15N	665.0	647.0–679.0	17 000	1028	52
HR21	875.7	434.0–458.7	18 470	284	55

release, we have RVs for 1028 GIRAFFE targets and 25 UVES targets.

The 25 UVES stars have well-defined values of effective temperature, surface gravity, and microturbulence derived directly from these spectra (summarised in Table 3). While elemental abundances are available for various elements in the GESviDR1Final data release, this work focused on the abundances of Fe, Al, Mg, Na, and Si (Table 4). The reference solar abundances used by GES are those of Grevesse et al. (2007).

Because the main-sequence targets are hot, fast-rotating stars, preliminary metallicity determinations from GIRAFFE are for the moment available for 255 GIRAFFE stars only in GESviDR1Final, with large quoted uncertainties. These data will be re-analysed in subsequent GES data releases. We have decided not to consider these results and to focus only on the metallicity determination obtained from the UVES spectra.

2.4. HARPS Archive data

We compared our results with those obtained using an HARPS archive data set taken by the program Search for Planets around Evolved Intermediate-Mass Stars (Lovis & Mayor 2007). Twenty-nine stars in the cluster have been monitored for a total of more than 70 h of on-target integrations and 271 spectra taken. The observing programme covered several periods from P79 (2007) to P83 (2009). In the ESO archive, the observed dataset is already reduced, providing a measure of the RVs. Owing to its high resolving power ($R \sim 115\,000$) and simultaneous wavelength calibration, HARPS delivers a typical radial velocity error of about 0.06 km s^{-1} for these stars. Nineteen of them stars were also observed by GES with the UVES instrument, allowing for a sanity check of our UVES measurements, but none were observed with GIRAFFE. Figure 6 shows a comparison between the RVs derived from UVES and HARPS spectra. The nominal uncertainty on the UVES RVs is 0.6 km s^{-1}. The measurements from UVES are systematically lower by 0.8 km s^{-1} on average, with a standard deviation of 0.4 km s^{-1}. We corrected for the differences in zero point between the GIRAFFE, UVES, and HARPS radial velocities when using them together later in this study.

3. Membership

The spectroscopic targets were photometrically selected to be likely cluster members, but this selection obviously includes a significant number of field stars, which can be separated from the cluster stars on the basis of their RVs. Figure 5 shows the RV distribution of the field stars expected from the Besançon model (Robin et al. 2003). We selected from the simulation the stars belonging to the bright main sequence region, with $B - V < 1.2$ and $V < 17$ (the region of the CMD covered by the majority of the GIRAFFE targets) and scaled the distribution so that its tails (RV < 20 km s^{-1} and RV > 50 km s^{-1}) contain the same number of objects as those of the observed distribution. The Besançon model reproduces the observed RV distribution of the background very well, while the signature of the cluster is clearly visible as a peak around 36 km s^{-1}.

We performed a membership determination for GIRAFFE and UVES stars independently.

3.1. Membership of the GIRAFFE stars

We determined the membership of the GIRAFFE stars from the HR15N radial velocities only, because of the good signal-to-noise ratio (S/N) of these spectra and because all 1028 GIRAFFE stars were observed with this setup. The analysis of the data obtained with the other gratings will be available in further data releases.

We applied a classical parametric procedure where the radial velocity distribution is fitted with two Gaussian components: one for the cluster members and one for the field stars. We followed the procedure described in Cabrera-Caño & Alfaro (1985), but only based on the RVs. The RVs of stars that were observed with different GIRAFFE gratings are the two-sigma clipped averages. The method computes the membership probabilities through an iterative method. The probability density function (hereafter PDF) model is defined as

$$\phi_i(v_i) = n_c \phi_{i,c}(v_i) + n_f \phi_{i,f}(v_i) \quad (1)$$

where n_c and n_f are the priors of the cluster member and field stars distributions, respectively, $\phi_i(v_i)$ is the PDF for the whole sample, and $\phi_{i,c}(v_i)$ and $\phi_{i,f}(v_i)$ are the PDFs for the cluster members and the field stars related to the ith star.

The membership probabilities are obtained making use of these PDFs and by using Bayes' theorem as follows:

$$P_c(v_i) = \frac{n_c \phi_{i,c}(v_i)}{\phi_i(v_i)} \quad (2)$$

where $P_c(v_i)$ is the probability of the ith star to be a cluster member. According to Bayes' minimum error rate decision rule, a threshold value of 0.5 minimises the misclassification. At the end of the analysis, 536 stars (out of 1028) have a membership probability higher than 0.5. The mean RV of these stars is 35.9 km s^{-1}, with a standard deviation of 2.8 km s^{-1}.

Undetected member binaries may have discrepant RVs and be classified as non-members by this procedure. Rigourously speaking, the RV distribution of the members may deviate from a Gaussian. The measured RVs of unresolved binaries are the combination of the motion of the centre of mass and of the orbital motion, and they tend to have larger uncertainties than isolated stars. The result of convolving a binary model with a normal distribution is a modification of the tails of the Gaussian, by extending and increasing them. Here some unresolved pairs may therefore be classified as non-members.

3.2. Membership of the UVES stars

We have stellar parameters and accurate metallicities for the 25 UVES targets of NGC 6705, including three stars that show a very discrepant RV and are not members of the clusters (see Fig. 7). A fourth star (18510093-0614564) has an outlying radial velocity of 41.4 km s^{-1}, even though its photometry is compatible with the other cluster members. As a possible explanation,

Table 2. Positions, *BV* photometry, radial velocities, and membership probabilities of the GIRAFFE targets.

Star	RA	Dec	*B*	*V*	RV	Membership probability
18505884-0614409	282.7452	−6.2447	15.161	14.642	34.3 ± 1.3	0.91
18505976-0616255	282.7490	−6.2738	14.808	14.314	31.8 ± 2.2	0.81
18505998-0617359	282.7499	−6.2933	14.695	14.247	37.4 ± 0.9	0.92
			...			
18514946-0620231	282.9561	−6.3398	19.767	18.475	120.7 ± 1.5	0.0

Notes. The full table (containing 1028 rows) is available at the CDS.

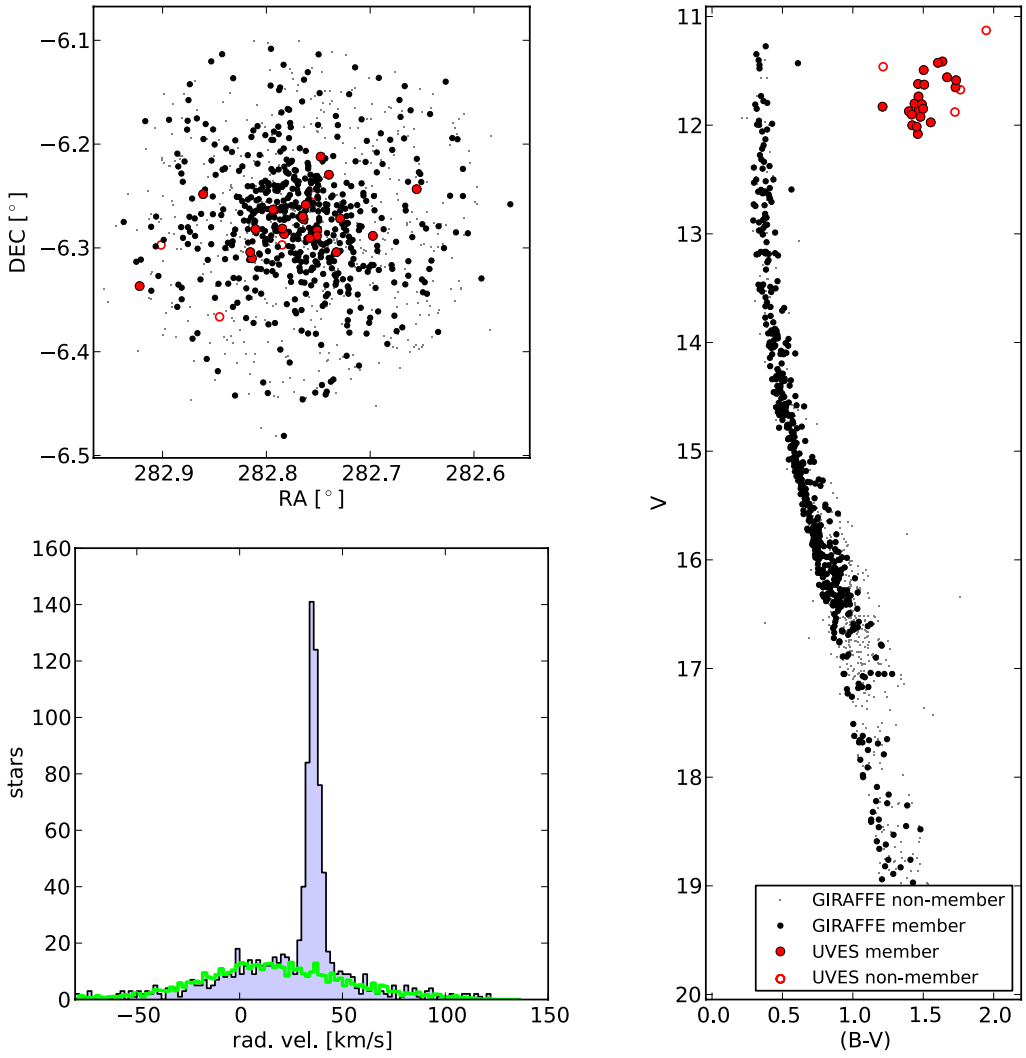

Fig. 5. *Top left*: positions of the GIRAFFE (black dots for members, grey points for non-members) and UVES targets (red dots for members, empy red symbols for non-members). *Bottom left*: radial velocity distribution of the GIRAFFE targets. The green line shows the expected radial velocity distribution of the field stars from the Besançon model (Robin et al. 2003). *Right*: CMD of all the GES stars.

this star could be a single-lined binary made of a red clump star and a main-sequence star. Being much hotter, the main-sequence companion contributes to the spectrum with only a continuum emission, making the lines shallower. This hypothesis would explain why this star has a discrepant radial velocity, and is also an outlier in metallicity, with [Fe/H] = −0.10 ± 0.10 (see following section). In the absence of further elements, we did not consider it as a member in the rest of this study.

Finally, 21 stars can be considered as bona-fide members of the cluster. The mean RV for the UVES members is 34.1 km s^{-1} (with a standard deviation of 1.5 km s^{-1}), which is lower than the mean value of 35.9 ± 2.8 km s^{-1} found for GIRAFFE stars. The lack of targets in common between both instruments do not allow for a solid comparison of the systematics between UVES and GIRAFFE, and both results are compatible within their standard deviations. In the first GES data release, Sacco et al. (2014) note an average offset of 0.87 km s^{-1} between the UVES and GIRAFFE HR15N radial velocities, which is consistent with the offset we observe here.

4. Extinction maps

When looking towards the inner parts of the Galaxy, the line of sight often meets regions of high extinction. Before discussing

Table 3. Photometry and stellar parameters of the UVES stars.

Star	RA [°]	Dec [°]	B	V	J	H	K_s	RV [km s^{-1}]	$T_{\rm eff}$ [K]	log g	[Fe/H]	$v_{\rm mic}$ [km s^{-1}]
Members												
18503724-0614364	282.6552	−6.2434	13.423	12.001	9.427	8.808	8.616	35.2	4820 ± 71	2.42 ± 0.21	0.03 ± 0.14	1.82 ± 0.13
18504737-0617184	282.6974	−6.2884	13.381	11.652	8.527	7.808	7.523	31.8	4325 ± 130	1.72 ± 0.29	0.03 ± 0.15	1.56 ± 0.16
18505494-0616182	282.7289	−6.2717	13.328	11.860	9.199	8.498	8.318	34.8	4689 ± 109	2.37 ± 0.43	0.13 ± 0.09	1.46 ± 0.12
18505581-0618148	282.7325	−6.3041	13.050	11.414	8.557	7.895	7.698	35.1	4577 ± 139	2.23 ± 0.31	0.17 ± 0.18	1.60 ± 0.24
18505755-0613461	282.7398	−6.2295	13.041	11.830	9.426	8.852	8.675	30.4	4873 ± 114	2.37 ± 0.32	0.03 ± 0.14	1.33 ± 0.19
18505944-0612435	282.7477	−6.2121	13.270	11.872	9.330	8.722	8.523	34.6	4925 ± 177	2.56 ± 0.39	0.19 ± 0.18	1.50 ± 0.50
18510023-0616594	282.7510	−6.2832	13.319	11.586	8.524	7.776	7.589	35.2	4433 ± 95	1.94 ± 0.47	0.17 ± 0.12	1.50 ± 0.14
18510032-0617183	282.7513	−6.2884	13.542	12.081	9.368	8.751	8.549	35.2	4850 ± 100	2.38 ± 0.21	0.07 ± 0.15	1.60 ± 0.33
18510200-0617265	282.7583	−6.2907	13.030	11.426	8.446	7.766	7.493	32.0	4415 ± 87	2.35 ± 0.45	0.18 ± 0.14	1.48 ± 0.07
18510289-0615301	282.7620	−6.2584	13.467	12.014	9.389	8.758	8.543	32.8	4750 ± 112	2.40 ± 0.28	0.05 ± 0.07	1.45 ± 0.13
18510341-0616202	282.7642	−6.2723	13.239	11.801	9.216	8.579	8.386	36.3	4975 ± 146	2.50 ± 0.30	0.07 ± 0.15	1.94 ± 0.27
18510358-0616112	282.7649	−6.2698	13.320	11.902	9.357	8.691	8.511	34.7	4832 ± 79	2.31 ± 0.31	0.15 ± 0.08	1.62 ± 0.19
18510786-0617119	282.7828	−6.2866	13.084	11.621	9.030	8.399	8.206	33.6	4768 ± 53	2.11 ± 0.19	0.03 ± 0.14	1.80 ± 0.28
18510833-0616532	282.7847	−6.2814	13.202	11.736	8.911	8.311	8.227	33.3	4750 ± 112	2.25 ± 0.22	0.18 ± 0.10	1.60 ± 0.25
18511013-0615486	282.7922	−6.2635	12.996	11.493	8.613	7.933	7.705	36.9	4439 ± 59	1.87 ± 0.53	0.10 ± 0.12	1.50 ± 0.10
18511048-0615470	282.7937	−6.2631	13.134	11.627	8.817	8.224	7.991	33.3	4744 ± 122	2.12 ± 0.33	0.05 ± 0.14	1.70 ± 0.30
18511452-0616551	282.8105	−6.2820	13.403	11.923	9.263	8.620	8.420	35.1	4800 ± 59	2.40 ± 0.25	0.11 ± 0.08	1.69 ± 0.20
18511534-0618359	282.8139	−6.3100	13.527	11.974	9.163	8.507	8.303	33.7	4755 ± 57	2.16 ± 0.21	0.05 ± 0.22	1.79 ± 0.17
18511571-0618146	282.8155	−6.3041	13.297	11.807	9.088	8.445	8.211	35.0	4710 ± 159	2.27 ± 0.30	0.15 ± 0.12	1.60 ± 0.18
18512662-0614537	282.8609	−6.2482	13.228	11.559	8.611	7.921	7.700	33.8	4459 ± 91	2.10 ± 0.48	0.12 ± 0.17	1.48 ± 0.19
18514130-0620125	282.9221	−6.3368	13.348	11.849	9.185	8.570	8.361	33.2	4671 ± 140	2.20 ± 0.28	0.07 ± 0.19	1.62 ± 0.20
Non-members												
18510093-0614564	282.7539	−6.2490	12.677	11.462	9.016	8.395	8.205	41.4	4755 ± 35	2.30 ± 0.24	−0.10 ± 0.10	1.50 ± 0.15
18510837-0617495	282.7849	−6.2971	13.438	11.674	8.469	7.649	7.429	−72.5	4217 ± 83	1.62 ± 0.33	−0.10 ± 0.12	1.47 ± 0.16
18512283-0621589	282.8451	−6.3664	13.604	11.879	8.831	8.084	7.872	3.4	4305 ± 95	2.08 ± 0.34	0.18 ± 0.18	1.61 ± 0.21
18513636-0617499	282.9015	−6.2972	13.075	11.128	7.295	6.451	6.127	−1.4	4041 ± 225	1.57 ± 0.42	−0.20 ± 0.20	1.45 ± 0.03

Notes. The photometry was not corrected for extinction. The nominal uncertainty on UVES radial velocities is 0.6 km s^{-1}.

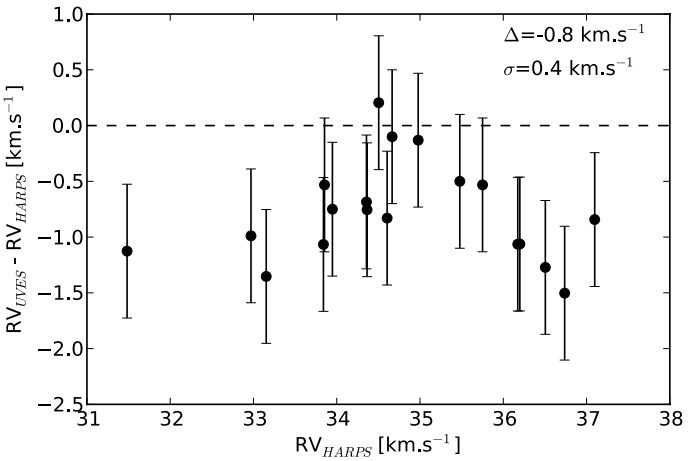

Fig. 6. Comparison between the radial velocity measurements from HARPS spectra and UVES spectra for 19 red giants.

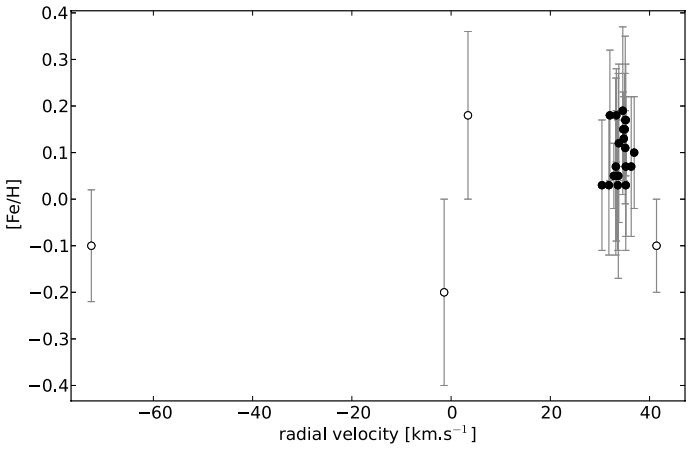

Fig. 7. Identification of the red clump cluster members from radial velocities and iron abundance. The error bars for the radial velocities are smaller than the symbols. The 21 filled circles correspond to the members, while the 4 open circles are the stars we consider non-members.

the age and the structure of NGC 6705, we need to assess whether the studied region is affected by differential extinction. The available VPHAS+ *ri* photometry covers a very wide field, much larger than our *BVI* photometry, which allows us to study the extinction of the background around the cluster. The *ri* CMD of the inner 12′ of the cluster is shown in Fig. 4. The PARSEC isochrone (Bressan et al. 2012) shown in that figure corresponds to the parameters of the best fit of the *BV* photometry (see Sect. 7). First we make use of the GIRAFFE members to derive the extinction law in the direction of the cluster. Figure 8 presents the colour-colour diagrams in the passbands *BVIri*. To fit the data, we need to adopt the relations $E(V-I) = 1.24(\pm0.05) \times E(B-V)$ and $E(r-i) = 0.68(\pm0.04) \times E(B-V)$. While the ratio $E(V-I)/E(B-V)$ is consistent with the total-to-selective extinction ratio $R_V = A_V/E(B-V) = 3.1$ using the Fitzpatrick (1999) law, the relation $E(r-i)/E(B-V)$ is slightly larger than the value of $E(r-i) = 0.6 \times E(B-V)$ given by Yuan et al. (2013).

Red clump stars in intermediate and old populations are often used in the literature as distance and extinction indicators.

Table 4. Elemental abundances for the UVES stars.

Star	[Fe/H]	[Al/Fe]	[Mg/Fe]	[Na/Fe]	[Si/Fe]
			Members		
18503724-0614364	0.03 ± 0.14	0.12 ± 0.15	0.23 ± 0.17	0.51 ± 0.17	0.09 ± 0.15
18504737-0617184	0.03 ± 0.15	0.17 ± 0.17	0.23 ± 0.15	0.74 ± 0.21	0.03 ± 0.17
18505494-0616182	0.13 ± 0.09	0.26 ± 0.09	0.14 ± 0.09	0.5 ± 0.11	0.07 ± 0.09
18505581-0618148	0.17 ± 0.18	0.10± 0.18	0.12 ± 0.20	0.32 ± 0.21	0.05 ± 0.19
18505755-0613461	0.03 ± 0.14	−0.04 ± 0.38	0.10± 0.15	0.52 ± 0.14	0.07 ± 0.15
18505944-0612435	0.19 ± 0.18	0.14 ± 0.18	0.14 ± 0.22	0.49 ± 0.19	−0.04 ± 0.19
18510023-0616594	0.17 ± 0.12	0.21 ± 0.12	0.20 ± 0.16	0.39 ± 0.13	0.02 ± 0.18
18510032-0617183	0.07 ± 0.15	0.20 ± 0.15	0.21 ± 0.18	0.53 ± 0.16	0.02 ± 0.16
18510200-0617265	0.18 ± 0.14	0.13 ± 0.15	0.16 ± 0.16	0.17 ± 0.14	0.02 ± 0.15
18510289-0615301	0.05 ± 0.07	0.22 ± 0.07	0.13 ± 0.13	0.53 ± 0.11	0.05 ± 0.09
18510341-0616202	0.07 ± 0.15	0.19 ± 0.15	0.30 ± 0.16	0.54 ± 0.17	−0.07 ± 0.17
18510358-0616112	0.15 ± 0.08	0.18 ± 0.08	0.12 ± 0.10	0.49 ± 0.10	0.07 ± 0.11
18510786-0617119	0.03 ± 0.14	0.25 ± 0.14	0.42 ± 0.14	0.58 ± 0.18	0.08 ± 0.18
18510833-0616532	0.18 ± 0.10	0.18 ± 0.10	0.19 ± 0.14	0.51 ± 0.13	−0.06 ± 0.12
18511013-0615486	0.10 ± 0.12	0.23 ± 0.12	0.23 ± 0.16	0.52 ± 0.15	0.07 ± 0.14
18511048-0615470	0.05 ± 0.14	0.23 ± 0.15	0.39 ± 0.14	0.54 ± 0.21	−0.03 ± 0.23
18511452-0616551	0.11 ± 0.08	0.15 ± 0.11	0.15 ± 0.29	0.55 ± 0.16	0.06 ± 0.11
18511534-0618359	0.05 ± 0.22	0.25 ± 0.22	0.33 ± 0.24	0.49 ± 0.23	0.08 ± 0.24
18511571-0618146	0.15 ± 0.12	0.20 ± 0.13	0.09 ± 0.17	0.45 ± 0.14	0.0 ± 0.13
18512662-0614537	0.12 ± 0.17	0.29 ± 0.17	0.24 ± 0.22	0.59 ± 0.21	0.13 ± 0.22
18514130-0620125	0.07 ± 0.19	0.21 ± 0.19	0.11 ± 0.21	0.45 ± 0.20	0.01 ± 0.20
μ	0.10 ± 0.04	0.20 ± 0.04	0.19 ± 0.05	0.48 ± 0.05	0.04 ± 0.04
σ	$0^{+0.04}$	$0^{+0.05}$	$0^{+0.07}$	$0^{+0.06}$	$0^{+0.05}$
			Non-members		
18510093-0614564	−0.10 ± 0.10	0.23 ± 0.11	0.11 ± 0.16	0.45 ± 0.13	0.07 ± 0.12
18510837-0617495	−0.10 ± 0.12	0.20 ± 0.12	0.28 ± 0.14	0.32 ± 0.12	0.02 ± 0.13
18512283-0621589	0.18 ± 0.18	0.27 ± 0.20	0.24 ± 0.20	0.38 ± 0.23	0.06 ± 0.20
18513636-0617499	−0.20 ± 0.20	0.53 ± 0.21	0.43 ± 0.20	0.41 ± 0.23	0.06 ± 0.21
Sun[a]	7.45	6.37	7.53	6.17	7.51

Notes. [(a)] The solar reference abundances are those of Grevesse et al. (2007). μ and σ are the intrinsic mean and dispersion, respectively (cf. Sect. 8).

The PARSEC isochrones indicate that the $r - i$ colour of the red clump varies by 0.07 for ages from 2 to 10 Gyr, and by 0.14 for Z from 0.001 to 0.03. The small dependence of their magnitude and colour on age and metallicity makes them good tracers of the extinction across the field.

We simulated a field corresponding to the coordinate of the cluster using the Padova Galaxy Model (Vallenari et al. 2006). The red clump stars in the model have an absolute r magnitude of 0.55 and an intrinsic colour $(r - i) = 0.525$. We followed the colour excess of the red clump stars at different distances. The field was divided into cells of $0.25° \times 0.25°$. In each of these cells, we computed the reddening as follows: the red giant stars falling in the magnitude range that corresponds to the distance range we want to probe (for instance, $11.5 < r < 13$ for 2−4 kpc) were divided into bins of 0.05 in the $(r - i)$ colour, and we looked for the most populated colour bin. This colour was then compared to the reference value of $(r - i) = 0.525$, to find the colour excess. We applied the procedure a second time, looking at a fainter magnitude slice, to take into account that one must look at fainter magnitudes to probe stars that are more reddened. We found that going for more iterations did not significantly change the results. After this second step, the final colour excess $E(r - i)$ was converted to $E(B - V)$ using the relation $E(r - i) = 0.68 \times E(B - V)$. Our bins of 0.05 in $r - i$ colour correspond to a resolution of 0.07 in $E(B - V)$. The extinction map we obtain for the distance range 2−4 kpc is visible in Fig. 9.

The inner region of the cluster studied with the WFI BVI photometry sits in a zone of relatively low and uniform extinction, with $E(B - V) = 0.40$ out to 11′ from the centre. A higher extinction is found at Dec $> -6°$and RA $< 283.25°$, with $E(B - V)$ up to 0.7. A comparison with the map by Schlegel (1998) shows consistency, with the north-west quadrant being the most reddened. However, the maps of Schlegel (1998) give the integrated extinction along the line of sight, while we restrict our determination to the distance range 2−4 kpc. For this reason, our values of extinction are lower, and the distribution is not directly comparable.

Although the cluster itself lies in a window of constant extinction, the bottom left-hand panel of Fig. 9 shows clearly that the star density distribution of the photometrically selected VPHAS+ cluster stars (Fig. 4) is correlated with the extinction, making the background density inhomogeneous.

In the bottom right-hand panel of Fig. 9 we show the distribution of photometrically selected stars from the 2MASS catalogue with $J < 15$ (Fig. 10). The infrared bands of the 2MASS data are less affected by extinction than the r and i bands of VPHAS+, and the relations by Yuan et al. (2013) tell us that a reddening of $E(B - V) = 0.7$ translates to an extinction of 0.54 mag in the J band. The distribution obtained for the 2MASS stars is similar to the one obtained for the VPHAS+ stars, with a hole in the distribution in the north-east quadrant and a steep drop in the stellar density in the north-west. Further details on this density

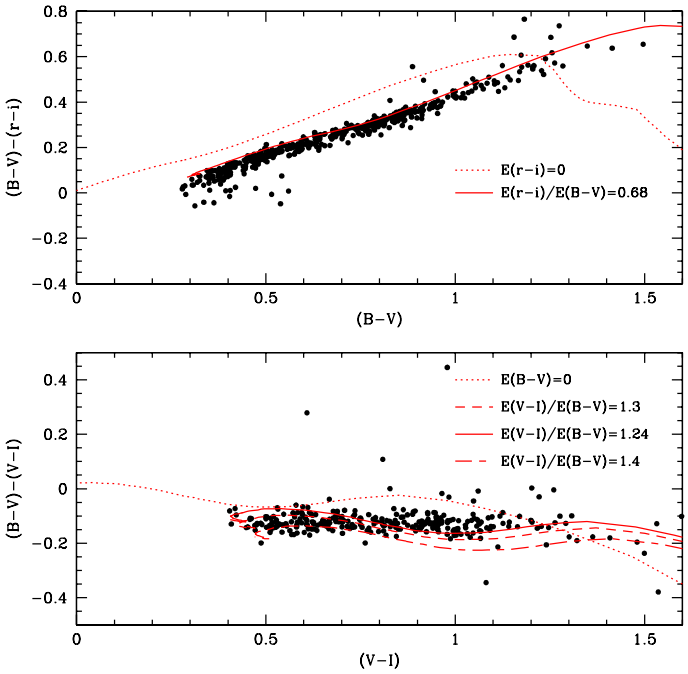

Fig. 8. Colour−colour diagrams on NGC 6705 GIRAFFE members main-sequence stars, compared with the relation expected from PARSEC isochrones for various extinction laws.

distribution are given when we establish the luminosity profile of the cluster (Sect. 5.2).

5. Cluster structure

To derive the cluster structure, we make use of the WFI photometry in the inner region and of the VPHAS+ data in the external parts.

5.1. Centre determination

To determine the position of the centre of the cluster, we first made a photometric selection that includes the brightest stars (red clump and upper main sequence). We used the method described by Donati et al. (2012) that consists in finding the barycentre of the sample, then retaining the 70% of the stars that lie closest to this barycentre and repeat the procedure until convergence to the actual centre of the cluster. The uncertainty on the final position arguably depends on the uncertainty in the selection of cluster members. Selecting only the brightest stars gives a better-defined membership but also poorer statistics. Using different magnitude cuts from $V = 13$ to 16, the position of the centre is at $\alpha_{2000} = 18^{\rm h}51^{\rm m}4^{\rm s}$, $\delta_{2000} = -6°16'22''$ (RA = 282.767°, Dec = −6.273°) with an uncertainty of 2″.

5.2. Radial density profile

We derived the luminosity profile using the V-band magnitudes. Through a χ^2 minimisation, we fitted a single mass two-parameter King profile (King 1962):

$$f(r) = \sigma_{\rm bg} + \frac{\sigma_0}{1 + (r/r_{\rm core})^2} \quad (3)$$

where $\sigma_{\rm bg}$ the background luminosity, σ_0 the central luminosity and $r_{\rm core}$ the core radius are left as free parameters.

The data was corrected for completeness in each radius and magnitude bin. Using all the stars with $V < 18$, we obtain a core radius of $1.23 \pm 0.28'$ (Fig. 11). This value is in agreement with the value of $1.81 \pm 0.71'$ found by Santos et al. (2005, hereafter S05) using main-sequence stars brighter than $J = 15$. Taking our distance estimate (Sect. 7.1) into account, we obtained a core radius of 0.69 ± 0.24 pc in physical units.

The much wider field offered by the VPHAS+ data enables us to trace the luminosity profile in the most distant parts of the cluster. We established the luminosity profiles in three different quadrants (Fig. 12). We can see that the three profiles are similar inside 10′, with the small differences explained by statistics and a patchy extinction, but show different behaviours at larger radii. As one could expect from the extinction map of Fig. 9, the luminosity in the north-west quadrant drops to lower values than in the other two. In the north-east quadrant, a dip is visible between 25′ and 40′, corresponding to a region of stronger extinction of the background (see Fig. 9). In the south-west quadrant, beyond 20′, the background density increases with radius as the extinction decreases. Since outside of the core the luminosity profile is mainly shaped by extinction, it is not possible to estimate the tidal radius of NGC 6705 by fitting a three-parameter King profile. The value of $r_{\rm tidal} = 52 \pm 27'$ reported by S05 falls exactly in the distance range affected by strong extinction. S05 also observed a deviation of the luminosity profile from their model between 11′ and 16′, and suggest this excess could be due to low-mass stars moving to larger radii due to mass segregation. Without a proper model for the background density, it seems very difficult to draw conclusions on the structure of the cluster beyond 10′.

5.3. Mass segregation from the luminosity profile

Mass segregation is an internal dynamical phenomenon that takes place in star clusters and leads the most massive stars to be more tightly clumped than the least massive ones (Spitzer 1969). A certain number of methods can be used to see whether mass segregation is occurring in a cluster, for instance applying a minimum spanning tree analysis (Allison et al. 2009), or directly comparing the distance to the centre for stars of different brightness. Here we compare the density profiles of stars in different mass ranges (cf. Sect. 5.2) and compare the slope of the mass function in different regions of the cluster (our Sect. 7.3, and S05).

Figure 13 shows the luminosity profiles established in four different magnitude ranges: 10−13, 13−15, 15−16, and 16−18. For our best-fitting PARSEC isochrone, these correspond to the mass ranges: $M > 2.14\,M_\odot$, 2.14−1.37, 1.37−1.14, and 1.14−0.81. For stars with $V > 16$, we applied a completeness correction based on the distance and magnitude.

In the faintest range ($16 < V < 18$) we discarded the data point corresponding to the most central bin ($r < 0.5'$), owing to the very low completeness for faint stars at the centre of the cluster. It is clear that the core radius increases as fainter stars are considered from $1.02 \pm 0.25'$ in the range $10 < V < 13$ to $3.62 \pm 1.12'$ in the range $16 < V < 18$. This result is consistent with results by Sung et al. (1999), although they do not quantify the increase in radius for the distribution of progressively fainter stars.

6. Kinematics

6.1. Rotation

Since NGC 6705 is a massive system and radial velocities are available for a large number of targets, we looked for hints of

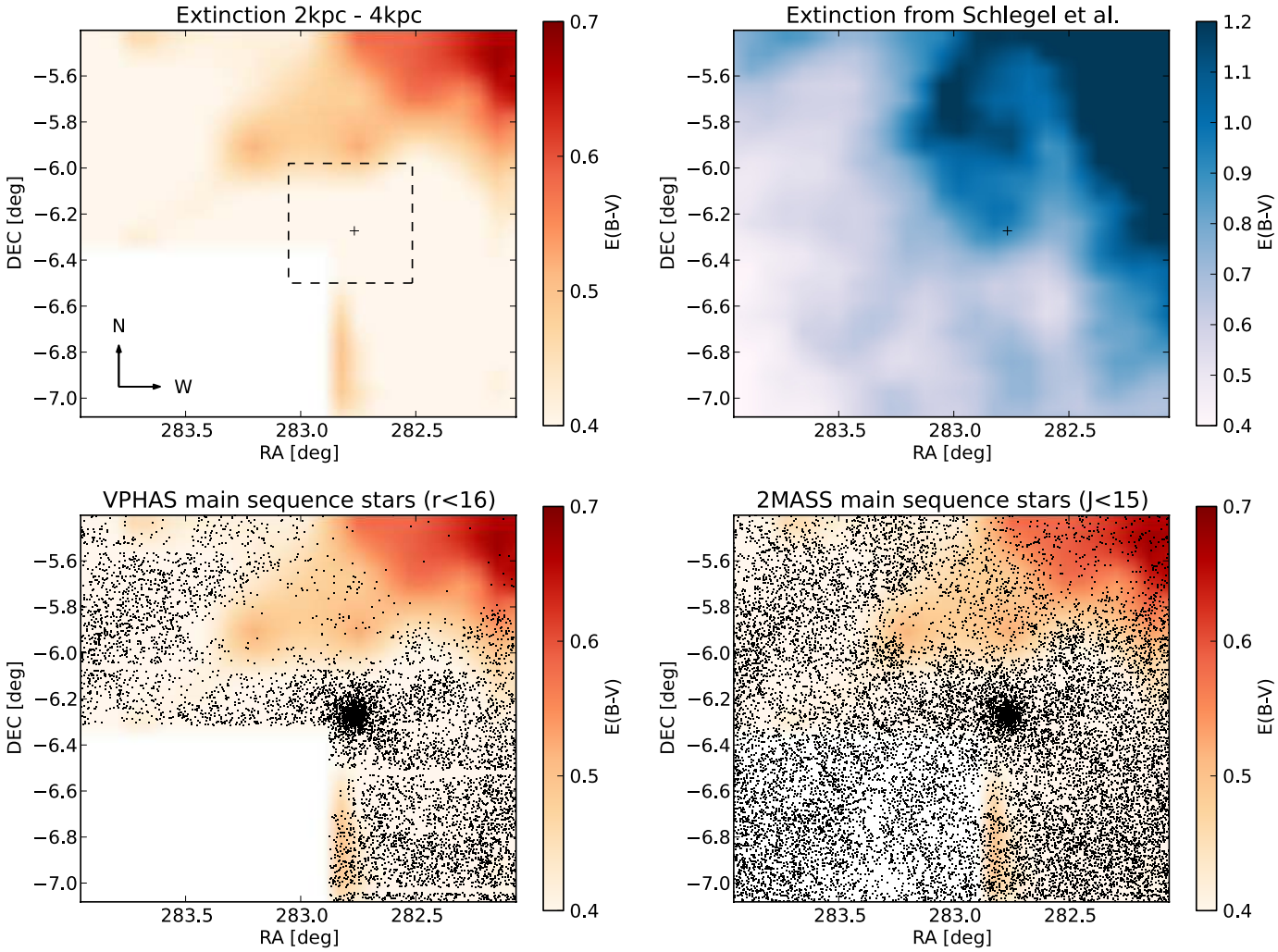

Fig. 9. *Top left*: extinction map obtained from VPHAS+ photometry in the distance range 2−4 kpc. The cross indicates the centre of the cluster. The dashed line shows the footprint of our *BVI* photometry. *Bottom left*: same extinction map. The black points are cluster stars selected from the $(r-i, r)$ VPHAS+ CMD, with $r < 16$. The CCD gaps are visible as horizontal lines. *Top right*: extinction map from Schlegel (1998) for this field. *Bottom right*: same as *bottom left*, but with 2MASS main-sequence stars ($J < 15$).

the rotational signature of the cluster, as is routinely done for GCs (see e.g. Cote et al. 1995; Bellazzini et al. 2012; Bianchini et al. 2013). We first corrected the GIRAFFE radial velocities for the offset observed in Sect. 2.4, then applied the procedure to the whole sample. The method consists in dividing the cluster in two and selecting one half according to a position angle ϕ measured here from north to east ($\phi = 0°$ corresponds to the north half, while $\phi = +90°$ and $\phi = -90°$ correspond to the east and west halves, respectively). The mean radial velocity is computed in the selected region. Varying the angle ϕ by steps of 5°, we trace the mean radial velocity in different regions. For a rotating object, we expect the radial velocities to follow a sinusoidal dependence on the position angle ϕ, being equal to the mean radial velocity of the cluster when ϕ corresponds to the orientation of the rotation axis (projected on the sky), following the equation

$$\Delta V_r = A_{\rm rot} \sin(\phi_0 + \phi) \quad (4)$$

where $A_{\rm rot}$ corresponds to the amplitude of the rotation and ϕ_0 is the position angle of the rotation axis. We estimated the uncertainty on the mean radial velocity by bootstrapping: in each position angle bin, containing N datapoints, we created 100 sets of N datapoints by randomly sampling the radial velocity dataset, calculated the mean velocity for each one, and computed the standard deviation of these results. The best-fitting sine function corresponds to an orientation angle $\phi_0 = 4 \pm 45°$ and an amplitude $A_{\rm rot} = 0.3 \pm 0.1\,{\rm km\,s^{-1}}$ around the mean radial velocity (Fig. 14). Since the RV is averaged over the full range of radii covered by the sample, the derived $A_{\rm rot}$ is a lower limit to the maximum rotation amplitude, depending on the rotational gradient of the cluster. The observed pattern is, however, very weak, with an amplitude much smaller than the velocity dispersion of the cluster, and we can conclude that rotation does not play a significant role in the observed velocity dispersion in NGC 6705.

6.2. Intrinsic velocity dispersion

Owing to uncertainties on the radial velocities of each invididual star, the velocity dispersions we observe in our samples ($2.8\,{\rm km\,s^{-1}}$ for the GIRAFFE sample, $1.5\,{\rm km\,s^{-1}}$ for the combined HARPS and UVES sample) are larger than the true, intrinsic dispersion of those stars. Assuming this intrinsic distribution is Gaussian, and that the quoted uncertainties $\{\epsilon_1, ..., \epsilon_N\}$ on the observed radial velocities $\{v_1, ..., v_N\}$ are Gaussian errors, it is possible to estimate the dispersion σ and the mean radial

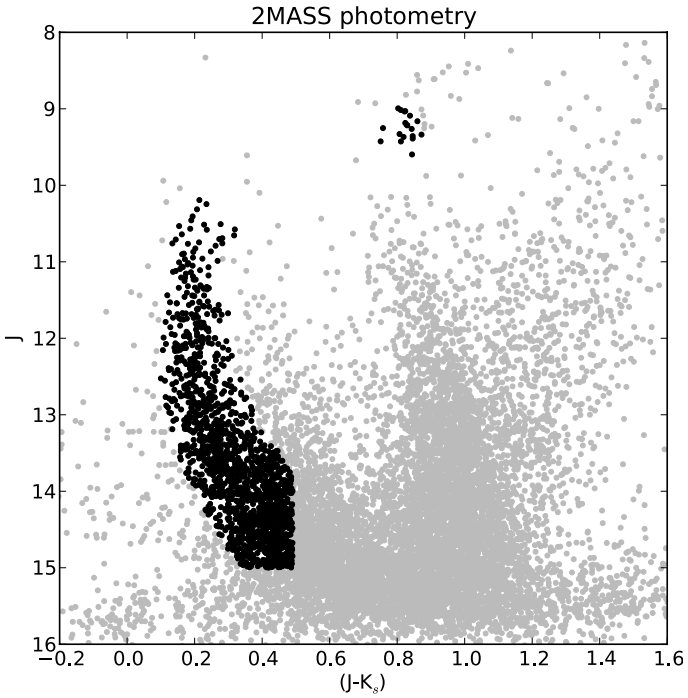

Fig. 10. 2MASS CMD of the inner 12′ of NGC 6705. The spatial distribution corresponding to the photometric selection (black points) is shown in Fig. 9 on a larger field.

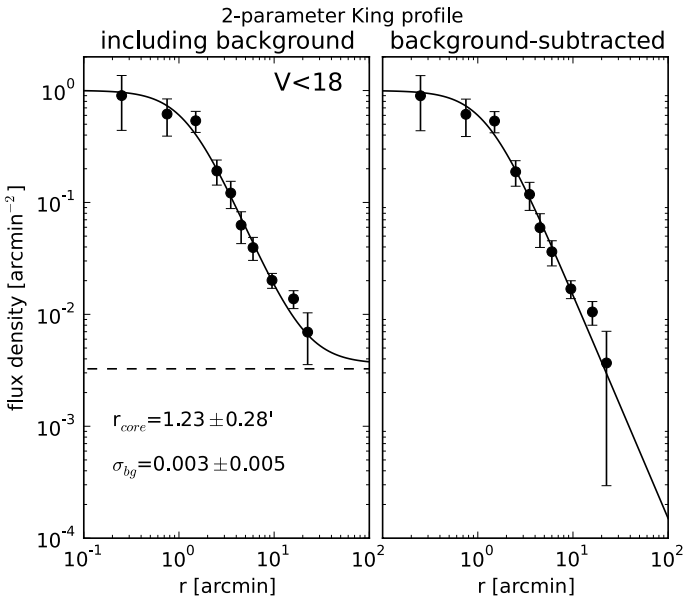

Fig. 11. Observed luminosity profile (black dots) for stars with $V < 18$, fitted with a two-parameter King profile (continuous line), including background (*left*) and after subtracting the background (*right*). The flux density was normalised to the central luminosity so that $\sigma_0 = 1$.

velocity μ of the true underlying distribution (see e.g. Walker et al. 2006).

The probability of measuring the radial velocity v_i by sampling a random point from a normal distribution that has mean μ and dispersion σ is

$$P(v_i, \mu, \sigma) = \frac{1}{\sqrt{2\pi\,(\sigma^2 + \epsilon_i{}^2)}} \exp\left(-\frac{1}{2}\frac{(v_i - \mu)^2}{\sigma^2 + \epsilon_i{}^2}\right). \quad (5)$$

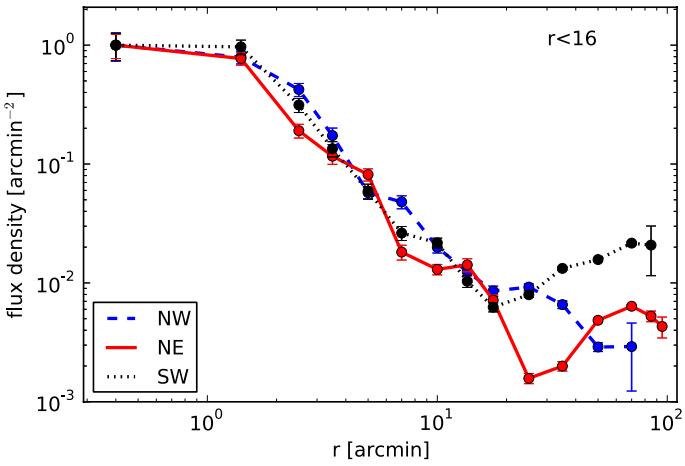

Fig. 12. Stellar density profiles for the north-west, north-east and south-west quadrants (NW, NE, and SW) of the VPHAS+ photometry, using stars with $r < 16$. The profiles in the three quadrants were normalised to the flux in the innermost bin. The background level was not subtracted.

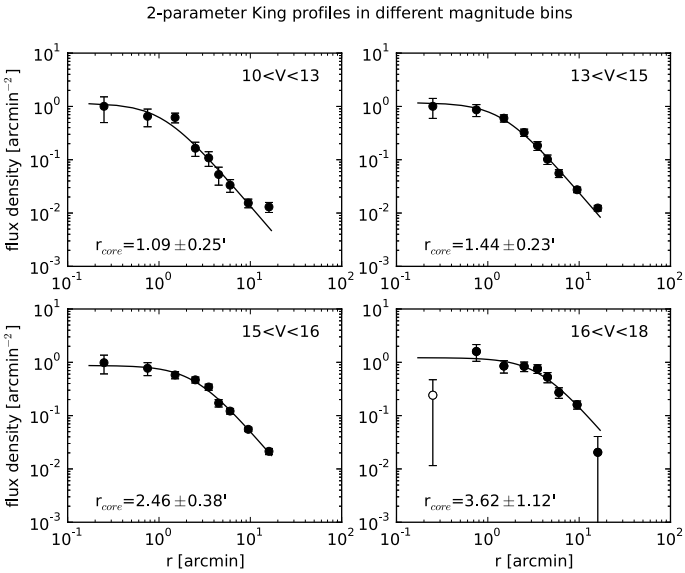

Fig. 13. Observed and fitted luminosity profiles obtained with stars in different magnitude ranges. The background was fitted and subtracted. In the *bottom right panel*, the open symbol is the datapoint that was discarded when fitting the luminosity profile.

For a sample of N stars, the joint probability is simply the product of the N individual probabilities:

$$\mathcal{L} = P(\{v_1, ..., v_N\}, \mu, \sigma) = \prod_{i=1}^{N} \frac{1}{\sqrt{2\pi\,(\sigma^2 + \epsilon_i{}^2)}} \exp\left(-\frac{1}{2}\frac{(v_i - \mu)^2}{\sigma^2 + \epsilon_i{}^2}\right) \quad (6)$$

and the best estimates of μ and σ are those that maximise $\mathcal{L}$. Applying this method to our sample of GIRAFFE RVs, we found the values $\mu_G = 36.0 \pm 0.2\,\mathrm{km\,s^{-1}}$ and $\sigma_G = 2.5 \pm 0.1\,\mathrm{km\,s^{-1}}$. For the HARPS+UVES sample, the results are $\mu_{H+U} = 34.8 \pm 0.4\,\mathrm{km\,s^{-1}}$ and $\sigma_{H+U} = 1.3^{+0.3}_{-0.2}\,\mathrm{km\,s^{-1}}$. We do not expect such large difference between the radial velocity dispersion of both samples. The most likely source of this difference is that the quoted uncertainties on the GIRAFFE radial velocities are underestimated. The GIRAFFE targets are hot, fast-rotating stars for which RVs can be difficult to measure, and the main source

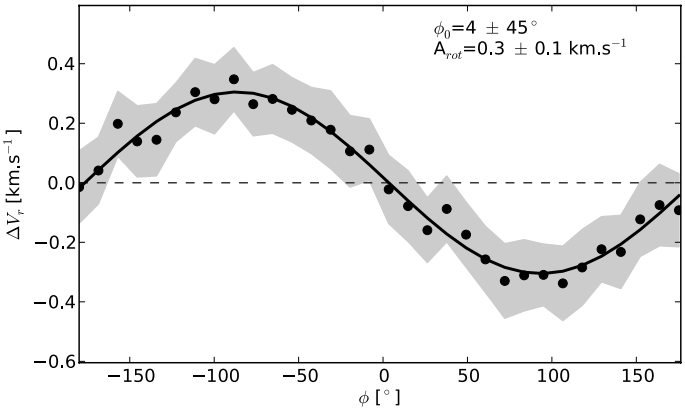

Fig. 14. Rotation curve obtained from the cluster members. The shaded region shows the uncertainty estimated via bootstrapping. The best-fitting sine corresponds to a position angle of the rotation axis $\phi_0 = 4°$ and an amplitude $A_{\rm rot} = 0.3\,{\rm km\,s^{-1}}$.

of dispersion in the GIRAFFE sample is likely to be the measurement errors. This hypothesis may be tested when the final analysis is available for all gratings in a later GES data release.

6.3. Virial mass

A complete kinematical study of the cluster would require proper motions and radial velocities for a significant share of the stars. We do not have such a dataset, but we have accurate radial velocities for 31 red clump stars of NGC 6705 (combining the HARPS and UVES datasets) that we can use to estimate a lower limit to the total mass of the cluster.

NGC 6705 exhibits mass segregation, which is a sign of a dynamically relaxed cluster, at least in its core. The mass of a dynamically relaxed cluster is related to its average radius and velocity dispersion through the virial theorem:

$$M_{\rm tot} = \frac{2\langle v^2\rangle\langle R\rangle}{G} \tag{7}$$

where G is the gravitational constant, $\langle R\rangle$ the average radius, and $\langle v^2\rangle = v_\mu^2 + v_\sigma^2 + v_r^2$ the three-dimensional velocity dispersion. In this study we only have access to the radial velocity dispersion v_r. However, assuming that the velocity distribution is isotropic, the three components of the velocity dispersion are equal and we can write

$$\langle v^2\rangle = v_\mu^2 + v_\sigma^2 + v_r^2 = 3v_r^2. \tag{8}$$

With $\sqrt{\langle v_r^2\rangle} = 1.34^{+0.32}_{-0.22}\,{\rm km\,s^{-1}}$ and an average radius $\langle R\rangle = 3.42'$ (2.0 ± 0.2 pc) (with the most distant star located at an agular distance of 10.1′) this equation yields $M_{\rm tot} = 5083 \pm 1600\,M_\odot$. The number is in good agreement with the virial mass obtained by McNamara & Sanders (1977) with the same method, but using proper motions ($5621\,M_\odot$). It is possible to plug in the values obtained from the GIRAFFE targets, which spread out to 12.6′ and show a larger average radial distance and a considerably higher velocity dispersion (4.52′ and $2.8\,{\rm km\,s^{-1}}$, respectively). The result is a mass of $21\,900 \pm 2700\,M_\odot$. Since the velocity dispersion of the GIRAFFE stars is affected by the larger uncertainty on the radial velocities, this value can be considered an upper limit.

This simple method only provides a first-order estimation. A more sophisticated approach would include detailed kinematical modelling, for instance adopting a multi-mass model approach as is generally done for GCs (see for instance Miocchi 2006). This is, however, beyond the scope of the paper. The calculation presented here only considers the positions and radial velocities of the massive stars in the central region and may suffer from biases due to the low number of selected targets. With a mass of the order of $5 \times 10^3\,M_\odot$ contained in the inner part (within 2 pc), we confirm that NGC 6705 is a relatively massive OC.

7. Age determination

In this section we give an estimate of the age, distance, and metallicity of NGC 6705 from the CMD analysis of the WFI photometry, which corresponds to the part of the cluster that is not affected by variable extinction. We first compared the CMD with PARSEC (Bressan et al. 2012) and Dartmouth (Dotter et al. 2008) isochrones, then proceeded to fit a synthetic luminosity function in the inner region of the cluster.

7.1. Comparison with theoretical isochrones

We have compared the BVI CMD of the inner 6′ of NGC 6705 with PARSEC and Dartmouth isochrones. The age, distance modulus, reddening and metallicity of the cluster can be estimated by matching the key features of the CMD (such as the main sequence slope and the positions of the main sequence turn-off and the red clump) traced by the cluster members established in Sect. 3.1 to the shape of the theoretical isochrones.

The PARSEC isochrone that reproduces best the morphology of the CMD is a model of 316 Myr ($\log t = 8.5$), solar metallicity ($Z = 0.0152$), $E(B-V) = 0.40$ and $(V - M_V) = 11.45$ ($d_\odot = 1995 \pm 180$ pc). The left-hand side panels of Fig. 15 show this isochrone, along with different choices of distance modulus, extinction, ages, and metallicities. Using a PARSEC isochrone of slightly super-solar metallicity produces a marginally compatible fit. On the other hand, a sub-solar metallicity fails to reproduce the position of both the red clump and the main sequence turn off at the same time. We estimate the uncertainty on the extinction to be of the order of 0.03, the uncertainty on the age 50 Myr. For an age of 316 Myr, the mass of the main sequence turn off stars is $3.2\,M_\odot$.

The best set of parameters for fitting a Dartmouth isochrone is an age of 250 Myr, extinction $E(B-V) = 0.37$, and distance modulus $(V - M_V) = 11.6$ ($d_\odot = 2090$ pc), as shown in Fig. 15. Again, using isochrones of super-solar metallicities produces a less satisfying fit than a solar metallicity. The age of 250 Myr is in agreement with the result of S05, who used Dartmouth isochrones on 2MASS photometry. This age corresponds to a turn off mass of $3.47\,M_\odot$. The best fits for these two sets of isochrones are both shown on Fig. 16 for a direct comparison.

As already discussed, PARSEC and Dartmouth isochrones give different determination of the age. This difference is due to the fact that the red clump stars tend to be brighter in the PARSEC tracks than in the Dartmouth tracks, because of a different choice of mixing-length parameter and solar metallicity reference (see Sect. 5.6 of Bressan et al. 2012). As a consequence, a PARSEC isochrone of higher age is needed to reproduce the position of the red clump.

To fit the $(V - I)$ colour in Fig. 16 we adopt the relation $E(V-I)/E(B-V) = 1.24$ derived in Sect. 4. Figure 17 shows the position of the 21 UVES cluster members in the ($T_{\rm eff}$ – $\log g$) plane. PARSEC isochrones of age 316 Myr and solar or slightly super-solar metallicity are compatible with the location of the red clump stars.

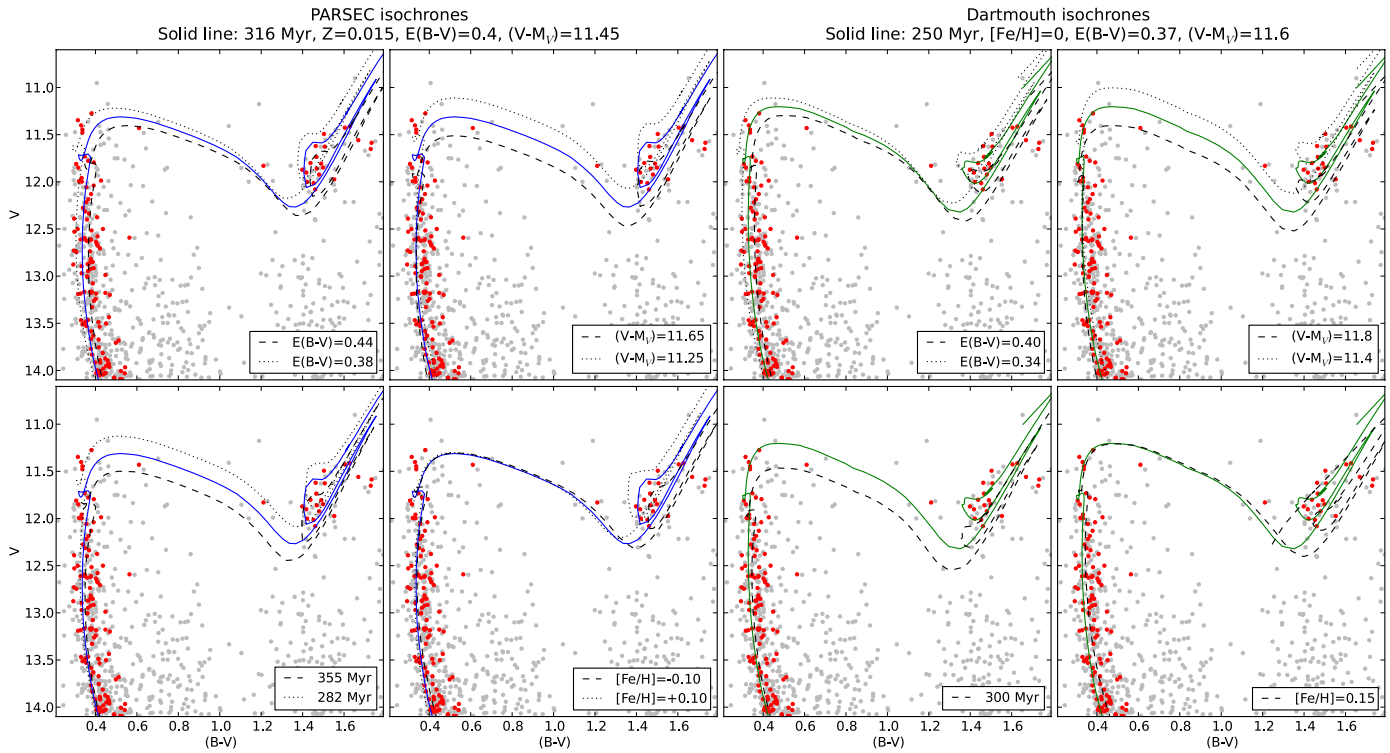

Fig. 15. Comparisons of the *BV* CMD with PARSEC and Dartmouth isochrones of various parameters. The grey points are all the stars in our photometry, and the radial velocity members are marked in red. *Left-hand side panels*: the best-fitting PARSEC isochrone (solid blue line) corresponds to an age of 316 Myr, a solar metallicity, a reddening $E(B-V) = 0.40$ and a distance modulus $(V - M_V) = 11.45$. The four panels show the change in the isochrone when modifying the extinction, distance modulus, age and metallicity with respect to the best-fitting isochrone. *Right-hand side panels*: same procedure with Dartmouth isochrones. The best-fitting isochrone is the solid green line. In all cases, the data are uncorrected for extinction. The isochrones are shifted along the extinction vector.

7.2. Luminosity function

To confirm the results obtained from the comparison with theoretical isochrones, we studied the luminosity function (LF) of the inner 0.1° (6′) of the cluster. This region is large enough to provide good statistics, without being too contaminated by background stars. A photometric selection was made, following the main sequence down to magnitude V=18. We considered the stars farther than 0.3° (18′) from the centre of the cluster as our background field (see Fig. 3). The LF of the background field was subtracted from the LF of the cluster, taking the respective completeness and area of the two regions into account. The error on the luminosity function takes the statistical error on both the cluster and the background into account.

Synthetic populations were computed using PARSEC tracks (Bressan et al. 2012), varying the age and metallicity, as well as the slope α of the initial mass function (IMF) and the distance modulus. The reddening was kept fixed to a value of $E(B-V) = 0.40$. The LF of the synthetic populations were compared with the observed LF using a χ^2 method and imposing a constrain on the colour of the main sequence and red clump.

Using isochrones of solar metallicity provide the lowest χ^2, and isochrones with [Fe/H] = +0.10 provide very similar results, while using [Fe/H] = −0.10 provides worse fits. The χ^2 maps (Fig. 18) show the confidence interval of the parameters that reproduce the observed LF. From these maps we estimate the parameters of the cluster as $\log t = 8.55 \pm 0.1$, $(V - M_V) = 11.55 \pm 0.3$, and the IMF slope $\alpha = 2.95 \pm 0.2$.

In this procedure, we did not take into account that some of the stars may be unresolved binary (or multiple) systems. Weidner et al. (2009) indicate that even in the extreme case where 100% of the stars are in multiple systems, the α parameter may be underestimated by 0.1 at most.

7.3. Mass function and total mass

In this section we derive the mass of the cluster using its LF. We produce the LF of the cluster in three annuli (corresponding to distance the ranges 0′−3′, 3′−6′, and 6′−9′) and convert the V magnitudes to masses using a PARSEC isochrone with the parameters determined in Sect. 7.1. The observed magnitude range ($V < 18$) corresponds to a mass range of 1 to 3.2 $M_\odot$. We chose to limit ourselves to the inner 9′. At larger radii, the cluster is hardly visible against the field stars, and our procedure that consists in subtracting the LF of the background from the observed one becomes very uncertain.

In each region, we derived the parameter α, defined as $N(M)\,\mathrm{d}M \propto M^{-\alpha}$. The results of the fit are shown in Fig. 19. The value of α increases with the radius, indicating that the mass function gets steeper because of a deficit of high-mass stars. In the most central region, $\alpha = 1.18$ indicates an excess of high-mass stars with respect to what would be expected from the Salpeter IMF ($\alpha = 2.35$). Over the whole range 0−9′, the slope of the mass function is $\alpha = 2.70 \pm 0.2$.

The previous studies of the evolution of the slope of the IMF with the radius have also found that the mass function was flatter in the inner region. S05 found a slope of $\alpha = 0.27$ in the inner 1.8′, $\alpha = 2.41$ in the region 1.8−10′, and $\alpha = 3.88$ in the region 10−21′. Sung et al. (1999) find slopes of $\alpha = 0.5$ to 1.7 inside 3′. The slope values found by those two studies are listed in Table 5 along with our estimates. The distance ranges given by S05 were

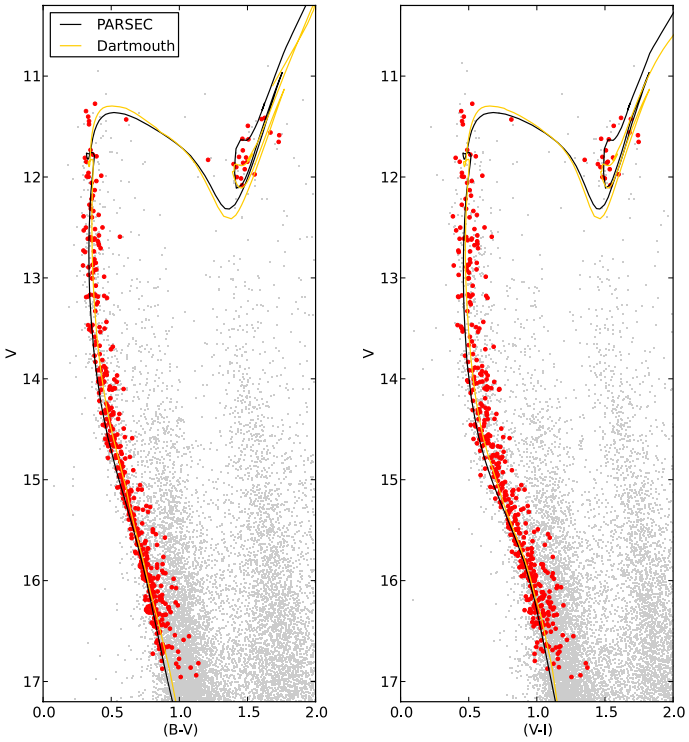

Fig. 16. Comparison between theoretical isochrones and our photometry (PARSEC isochrone of solar metallicity, 316 Myr, shifted by $E(B-V) = 0.40$ and $(V-M_V) = 11.45$ and Dartmouth isochrone of solar metallicity, 250 Myr, $E(B-V) = 0.37$, $(V-M_V) = 11.6$). The grey points are all the stars in our photometry, while the red points are the radial velocity members.

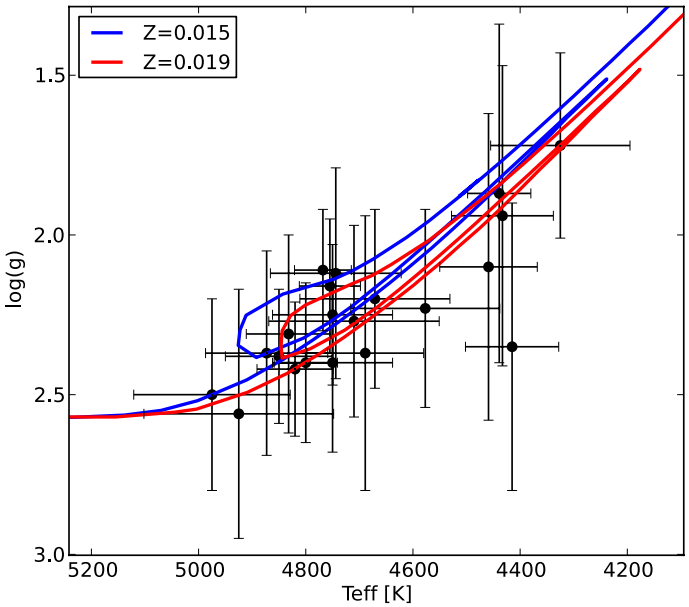

Fig. 17. Position of the 21 UVES members in the theoretical plane. The position of the red clump is reproduced well with a PARSEC isochrone of age $\log t = 8.5$ and $Z = 0.015$ ([Fe/H] = 0) or $Z = 0.019$ ([Fe/H] = 0.1).

converted back from parsecs to arcminutes using their value of the distance.

In theory, if the mass function of a cluster is known for its brightest stars, it is possible to extrapolate the mass functions down to lower masses and estimate the total stellar mass contained in the cluster. When dealing with mass-segregated OCs that were possibly affected by evaporation and tidal mass loss, inferring the mass function from the observed range to the lower masses is affected by large uncertainties. To obtain the slope of the mass function in the unobserved range (under 1 $M_\odot$) we used two methods. The simplest one is to assume that the slope of the power law derived from the stars with $M < 1\,M_\odot$ is the same over the full mass range. The second one is to use the IMF by Kroupa et al. (2001): $\alpha = 1.3$ for $0.08 < M_\odot < 0.5$ and $\alpha = 2.3$ for $0.5 < M_\odot < 1$. For masses over 1 $M_\odot$ we used the values obtained from our fit. In the inner region ($r < 3'$), we observe a nearly flat mass function, which means that using this slope over the whole mass range produces fewer low-mass stars than using the Kroupa IMF. In the other two regions, the mass function is steeper, and in the low-mass range it is well over the prediction of the Kroupa IMF. The result of integrating these mass functions are shown in Table 6 for the different choices of mass function in the different regions.

When integrating the mass function over the whole 0–9′ region, we obtained values between 3683 ± 1063 $M_\odot$ (using the Kroupa IMF under 1 $M_\odot$) and 6851 ± 1865 $M_\odot$ (using the extrapolated power-law). This latter number is compatible with the number quoted by S05, who estimate a total mass of 6500 ± 2100 $M_\odot$ inside 10′, and 11 000 ± 3800 $M_\odot$ inside 21′ using the IMF slopes listed in Table 6, and the Kroupa IMF under 1 $M_\odot$). Our determination does not take the presence of binary stars whose percentage is unknown into account. The effect of the presence of unresolved binaries on the observed α parameter is weak, but according to Weidner et al. (2009), not accounting for the presence of multiple systems can hide 15 to 60% of the stellar mass of a cluster. In addition, less massive stars could be either lost from the cluster due to the effect of the disk tidal field, or located in a surrounding halo. For these reasons, our determination is a lower limit to the cluster mass. Owing to the large uncertainties on the determinations, the derived values of the mass of NGC 6705 are in reasonable agreement with the virial masses derived in Sect. 6.3.

Table 5. Slope of the mass function in different regions on the cluster.

Radius (′)	α
This study	
0–1.8	0.50 ± 0.15
0–3	1.18 ± 0.11
3–6	3.01 ± 0.11
6–9	3.79 ± 0.10
0–9	2.70 ± 0.19
1.8–9	3.29 ± 0.07
Santos et al. (2005)	
0–1.8	0.27 ± 0.15
1.8–10	2.41 ± 0.10
10–21	3.88 ± 0.20
0–21	2.49 ± 0.09

Notes. α is the parameter in the mass function: $N(M)\,\mathrm{d}M \propto M^{-\alpha}$.

8. Chemical analysis of the red clump stars

The average iron abundance of the bona-fide members from UVES spectroscopy is [Fe/H] = 0.10 with a dispersion of 0.06. This value agrees with Gonzalez & Wallerstein (2000), who found iron abundances between 0.07 and 0.20 from high-resolution spectroscopy of ten K giants of NGC 6705 and with

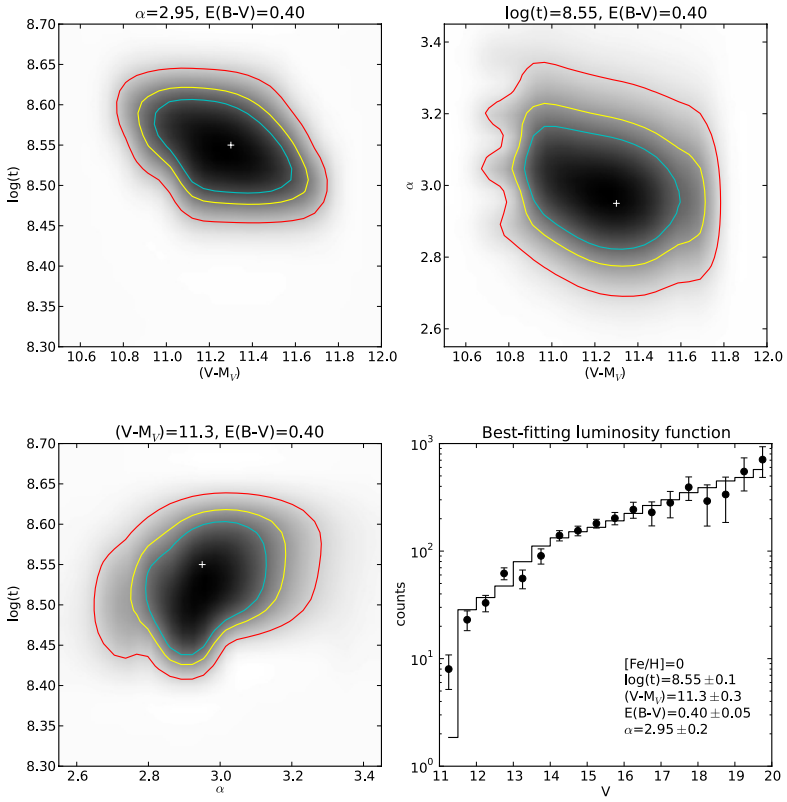

Fig. 18. Probability contours for the fit of the luminosity function. The cyan, yellow, and red lines show the 50%, 68%, and 90% confidence regions, respectively. The white cross indicates the best-fitting solution. The *bottom right panel* shows the observed LF (cleaned from the background) and the best-fitting theoretical one. The bins with $V > 18$ are shown but were not used in the fitting procedure.

Table 6. Mass contained in different regions of the cluster.

Region [′]	α	Observed [$M_\odot$]	Extrapolated (power law) [$M_\odot$]	Extrapolated (Kroupa) [$M_\odot$]
0–3	1.18 ± 0.11	242 ± 64	375 ± 56	664 ± 115
3–6	3.01 ± 0.11	241 ± 46	4303 ± 1127	1430 ± 151
6–9	3.79 ± 0.10	181 ± 43	18 888 ± 4702	1437 ± 242
Total		664 ± 153	26 566 ± 5885	3531 ± 508
0–9	2.70 ± 0.19	700 ± 310	6851 ± 1865	3683 ± 1063

Notes. α is the parameter in the mass function: $N(M)\,\mathrm{d}M \propto M^{-\alpha}$. The stars were observed down to 1 $M_\odot$. The extrapolation was done down to 0.08 $M_\odot$.

the values we derived from isochrone fitting. In this section we study the relations between the abundances of Al and of other proton-capture elements Na, Mg, and Si. Al and Na abundances are plotted against $T_{\rm eff}$ and log g in Fig. 20. These abundances do not display any significant trend. We observe star-to-star variations in the Al and Na content of the order of 0.2 dex, inside the expected uncertainties. Similar diagnostics for Mg and Si are shown in Magrini et al. (2014).

Abundances of Al, Mg, Si, and Na are plotted in Fig. 21. In case of multiple populations, correlations between the abundances of Al and Si, and between Al and Na, and anti-correlations between Si and Mg and between Al and Mg (Gratton et al. 2012) can be found. Models predict that Al should show correlations with elements that are enhanced by the action of the Ne–Na (such as Na) and Mg–Al cycles, and is anti-correlated with elements that are depleted in H burning at high temperature (such as O and Mg). We do not see any sign of such (anti-)correlations within our uncertainties.

One star shows a low Al abundance with a large uncertainty, with [Al/Fe] = −0.04 ± 0.38, probably due to the low number of detected lines for this element. Two outliers in Na abundance could suggest an internal spread, but they are still compatible with a homogeneous cluster within the uncertainties. The star with the highest Na abundance ([Na/Fe] = +0.74 dex) has the lowest Fe abundance in the sample ([Fe/H] = +0.03 dex), while the star with the lowest Na content ([Na/Fe] = +0.17 dex) has a Fe content [Fe/H] = +0.18 dex. This suggests that the apparent discrepant [Na/Fe] for that star can be explained by considering the uncertainties on both Na and Fe abundances.

The mean [Na/Fe] for the cluster members is 0.48 dex. This value is significantly higher than the Na abundance derived in field stars. Soubiran & Girard (2005) show that at high metallicities thin disk stars exhibit an average of [Na/Fe] = 0.11 dex, even though they notice a rise at super-solar metallicities. For all elements presented here, the abundances were calculated in the LTE approximation. Na is subject to deviations from LTE (e.g. Lind et al. 2011). The effect of non-LTE correction in stars of super-solar metallicity is expected to be small, but could lower the Na abundance of our sample by 0.15–0.20 dex at most. On a side note, since the corrections depend on the evolutionary stage of the star, we expect them to affect all of the red clump stars in the same way and not to create an additional spread in Na.

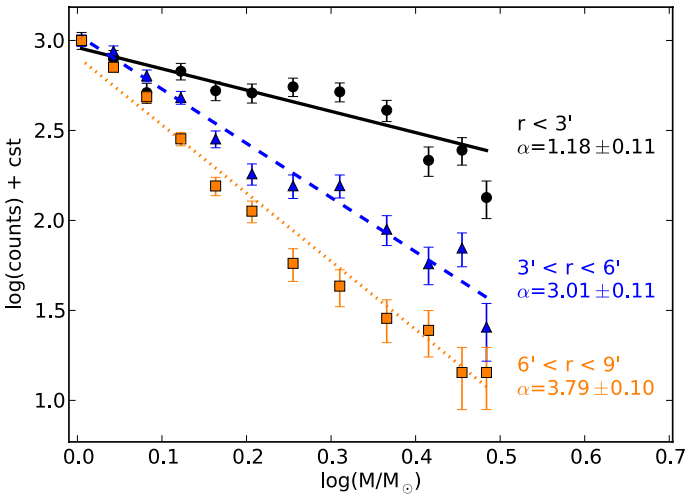

Fig. 19. Mass functions obtained in three different regions of the cluster, showing the flattening of the IMF in the centre. The y-axis was shifted so that the observed number of stars in the lowest mass bin is the same for all three.

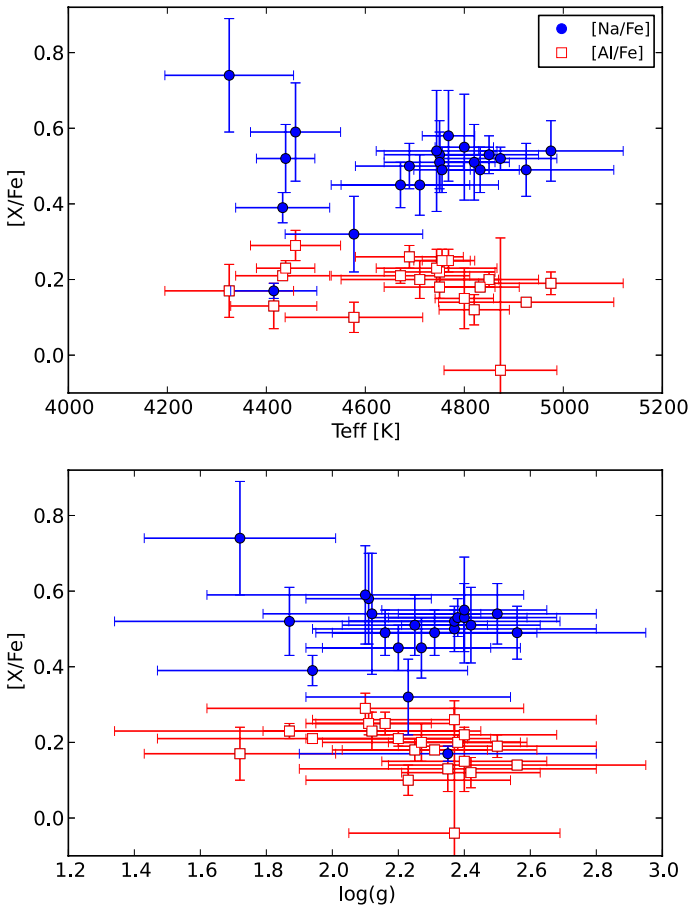

Fig. 20. Solar-scaled abundances of [Na/Fe] (blue filled dots) and [Al/Fe] (red open squares) for the 21 UVES member stars, as a function of $T_{\rm eff}$ and log g.

The approach presented in Sect. 6.2 to estimating the intrinsic radial velocity dispersion of the sample can also be applied to the elemental abundances. Assuming an intrinsic Gaussian distribution of the abundance for each element, the most probable mean abundance (μ) and intrinsic dispersion (σ) we computed are listed in Table 4. For all five elements, the observed distribution is compatible with the cluster being homogeneous, and the observed spread can be entirely attributed to the individual uncertainties.

As far as we can see, NGC 6705 is clearly a homogeneous object where the star-to-star scatter is explained by the uncertainties on the determination of the chemical abundances. Observationally, Carretta et al. (2010) suggests that clusters above a certain mass limit would develop multiple populations, and they derive the minimum (present-day) threshold mass of about $4 \times 10^4\,M_\odot$. On the theoretical ground, by comparing the timescale of the mixing of heavy elements in protoclusters with the cluster formation timescale, Bland-Hawthorn et al. (2010) suggest that clusters up to $\sim 10^4\,M_\odot$ masses, and possibly a significant fraction of those as massive as $\sim 10^5\,M_\odot$, should be chemically homogeneous. As we have seen, the mass of NGC 6705 is lower than $10^4\,M_\odot$ (see Sect. 7.3). This mass is still well under the expected $4 \times 10^4\,M_\odot$ mass threshold. Figure 3 in Carretta et al. (2010) (updated in Bragaglia et al. 2013) shows that the least massive GC known to present multiple populations is Pal 5, with a mass of $6.3 \times 10^4\,M_\odot$. Terzan 7 and Pal 12, with masses of $3.9 \times 10^4\,M_\odot$ and $2.8 \times 10^4\,M_\odot$ (respectively) do not show multiple populations. Owing to its mass, the chemical homogeneity of NGC 6705 and the lack of the element correlations expected in clusters showing multiple populations is consistent with the mass being the driving factor of cluster chemical evolution. However, the properties of M 11 differ in several respects from most GCs: it is younger, has a supra-solar metallicity (it is much more metal-rich than Pal 5, the least massive GCs known to contain multiple populations), and likely formed in a very different environment. While the lack of chemical inhomogeneities in M 11 confirms the above scenario, it cannot completely rule out alternative possibilities. However, this result needs to be verified on a larger sample.

9. Summary

We have used wide-field photometry from the ESO WFI and from the VPHAS+ Survey, together with spectroscopic data derived in the framework of the GES, to study the inner-disk cluster NGC 6705. We derived the extinction and the extinction law in front of the cluster. While the ratio $E(V-I)/E(B-V)$ is consistent with the total-to selective extinction ratio $R_V = A_V/E(B-V) = 3.1$ using the Fitzpatrick (1999) law, the relation $E(r-i)/E(B-V)$ is slightly higher than the value of $E(r-i) = 0.6 \times E(B-V)$ given by Yuan et al. (2013). Using the red clump stars as tracers, we derive the extinction for the distance range 2–4 Kpc, where the cluster is located. The inner region of the cluster studied with the WFI BVI photometry sits in a zone of relatively low and uniform extinction with $E(B-V) = 0.40$ out to 11′ from the centre. A higher extinction is found in the north-west quadrant, with $E(B-V)$ up to 0.7.

We attributed membership probabilities to the 1028 main-sequence stars for which radial velocities were available from the GES. We estimated the age of the cluster between 250 and 316 Myr depending on the adopted set of stellar isochrones. Its distance modulus turns out to be 11.45 ± 0.2 ($d_\odot$ = 1950 ± 200 pc). By fitting a two-parameter King profile, we find a core radius of 1.23 ± 0.28′ (0.69 ± 0.23 pc). The brightest stars of the cluster show a tighter spatial distribution, while the faintest stars are more widely distributed. Studying the mass function in different regions of the cluster showed that the inner parts contain a larger proportion of massive stars than the outer

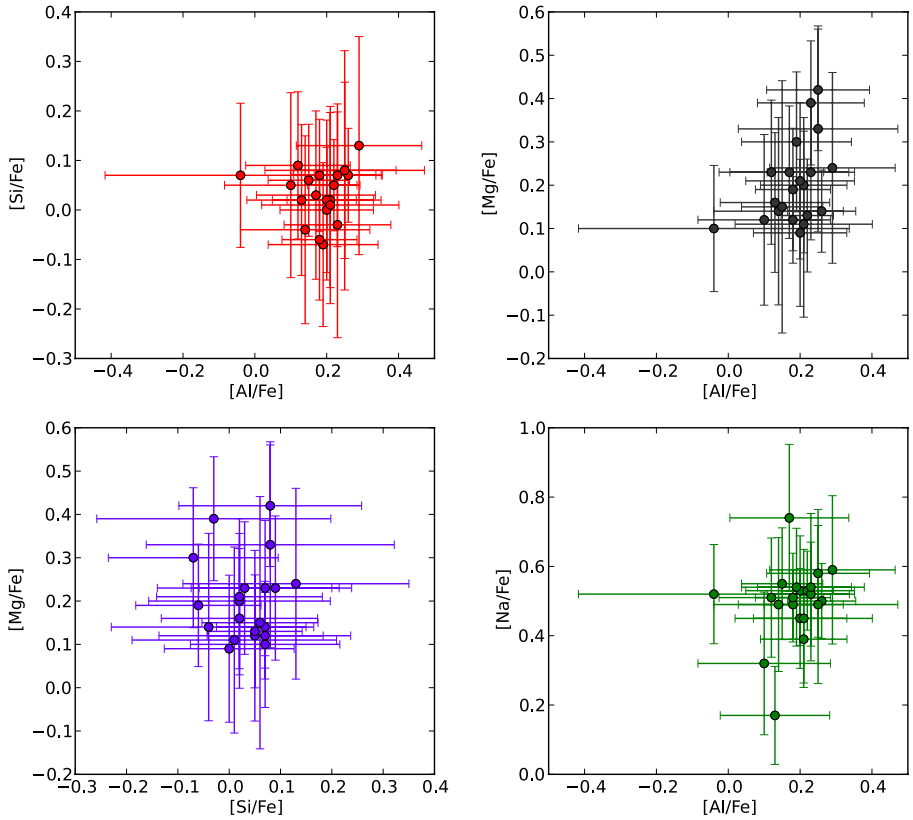

Fig. 21. Abundances of Al, Si, Mg and Na for the 21 red clump stars. None of the "classical" correlations or anti-correlations between elemental abundances are observed in this cluster, which seems chemically homogeneous within our uncertainties.

parts, confirming that NGC 6705 is undergoing mass segregation. Using the velocity dispersion of the sample of members stars observed by the GES consortium using UVES, we derived the virial mass of $M_{\rm tot} = 5083 \pm 1600\,M_{\odot}$, in agreement with the virial mass of 5621 $M_{\odot}$ found by McNamara & Sanders (1977) using proper motions. The sample of stars observed by GIRAFFE over a larger radius presents considerably higher velocity dispersion (4.52′ and 2.8 km s^{-1}, respectively). This sample leads to a virial mass of 21 900 ± 2700 $M_{\odot}$. However, the uncertainties on the GIRAFFE RVs are most likely underestimated, and this high virial mass must be considered an upper limit. We estimated a mass from photometry, converting the V-band luminosity function to a mass function. When integrating the mass function of the whole 0–9′ region, we obtain values between 3683 ± 1063 $M_{\odot}$ (using the Kroupa IMF under 1 $M_{\odot}$) and 6851 ± 1865 $M_{\odot}$ (using the extrapolated power-law).

The GES data enabled us to study the chemical composition of the red clump stars. We found an iron abundance [Fe/H] = 0.10 with a dispersion of 0.06. Despite being a massive open cluster, NGC 6705 does not show any sign of an inhomogeneous stellar population of the kind observed in globular clusters. This cluster is well below the mass limit of $4 \times 10^4\,M_{\odot}$ proposed in the literature for clusters hosting multiple populations. However, few massive clusters have been observed with high-resolution spectroscopy, and more studies are needed in order to observationally confirm this mass threshold.

The reliability of the results that can be obtained for stellar clusters greatly depends on membership determination and chemical abundances in the inner regions and in the outskirts, where haloes of unbound stars can be present. This especially holds for open clusters, which are more affected by the tidal field of the disks and by background contamination. The synergy between the GES and the ground-based surveys in general and the *Gaia* mission will provide invaluable information on the chemical abundances, distances and proper motions of unbiased samples of stars, allowing for more accurate determinations of the cluster properties.

Acknowledgements. Based on data products from observations made with ESO Telescopes at the La Silla Paranal Observatory under programme ID 188.B-3002. This work was partially supported by the *Gaia* Research for European Astronomy Training (GREAT-ITN) Marie Curie network, funded through the European Union Seventh Framework Programme (FP7/2007-2013) under grant agreement No. 264895, partly supported by the European Union FP7 programme through ERC grant number 320360 and by the Leverhulme Trust through grant RPG-2012-541. We acknowledge the support from INAF and the Ministero dell' Istruzione, dell'Università e della Ricerca (MIUR) in the form of the grants "Premiale VLT 2012" and "The Chemical and Dynamical Evolution of the Milky Way and Local Group Galaxies" (prot. 2010LY5N2T). The results presented here benefit from discussions held during the *Gaia*-ESO workshops and conferences supported by the ESF (European Science Foundation) through the GREAT Research Network Programme. This work was supported in part by the National Science Foundation under Grant No. PHYS-1066293 and the hospitality of the Aspen Center for Physics during summer 2013. L.S. aknowledges the support of Project IC120009 "Millennium Institute of Astrophysics (MAS)" of Iniciativa Científica Milenio del Ministerio de Economía, Fomento y Turismo de Chile. T.B. was funded by grant No. 621-2009-3911 from The Swedish Research Council. I.S.R. gratefully acknowledges the support provided by the Gemini-CONICYT project 32110029. S.V. gratefully acknowledges the support provided by FONDECYT N. 1130721. The authors wish to thank M. Bellazzini for his suggestions and comments that helped improve this work.

References

Allison, R. J., Goodwin, S. P., Parker, R. J., et al. 2009, MNRAS, 395, 1449
Bastian, N., & Silva-Villa, E. 2013, MNRAS, 431, L122
Bastian, N., Lamers, H. J. G. L. M., de Mink, S. E., et al. 2013, MNRAS, 436, 2398
Bellazzini, M., Bragaglia, A., Carretta, E., et al. 2012, A&A, 538, A18
Bianchini, P., Varri, A. L., Bertin, G., & Zocchi, A. 2013, ApJ, 772, 67

Bland-Hawthorn, J., Karlsson, T., Sharma, S., Krumholz, M., & Silk, J. 2010, ApJ, 721, 582
Bragaglia, A., Gratton, R. G., Carretta, E., et al. 2012, A&A, 548, A122
Bragaglia, A., Sneden, C., Gratton. R.G., Carretta, E., & Lucatello, S. 2013, ApJ, submitted
Bressan, A., Marigo, P., Girardi, L., et al. 2012, MNRAS, 427, 127
Cabrera-Cano J., Alfaro E. J., 1985, A&A, 150, 298
Carretta, E., Bragaglia, A., Gratton, R. G., et al. 2009a, A&A, 505, 117
Carretta, E., Bragaglia, A., Gratton, R. G., & Lucatello, S. 2009b, A&A, 505, 139
Carretta, E., Bragaglia, A., Gratton, R. G., et al. 2010, A&A, 516, A55
Carretta, E., Bragaglia, A., Gratton, R. G., et al. 2013, A&A, 561, A87
Cote, P., Welch, D. L., Fischer, P., & Gebhardt, K. 1995, ApJ, 454, 788
Decressin, T., Meynet, G., Charbonnel, C., Prantzos, N., & Ekström, S. 2007, A&A, 464, 1029
D'Ercole, A., Vesperini, E., D'Antona, F., McMillan, S. L. W., & Recchi, S. 2008, MNRAS, 391, 825
Donati, P., Bragaglia, A., Cignoni, M., Cocozza, G., & Tosi, M. 2012, MNRAS, 424, 1132
D'Orazi, V., Lucatello, S., Gratton, R., et al. 2010, ApJ, 713, L1
Drew, J. E., Gonzalez-Solares, E., Greimel, R. et al. 2014, MNRAS, 440, 2036
Dotter, A., Chaboyer, B., Jevremović, D., et al. 2008, ApJS, 178, 89
Fitzpatrick E. L., 1999, PASP, 111, 6
Geisler, D., Villanova, S., Carraro, G., et al. 2012, ApJ, 756, L40
Gilmore, G., Randich, S., Asplund, M., et al. 2012, The Messenger, 147, 25
Gonzalez, G., & Wallerstein, G. 2000, PASP, 112, 1081
Gratton, R. G., Bonifacio, P., Bragaglia, A., et al. 2001, A&A, 369, 87
Gratton, R., Sneden, C., & Carretta, E. 2004, ARA&A, 42, 385
Gratton, R. G., Carretta, E., & Bragaglia, A. 2012, A&ARv, 20, 50
Grevesse, N., Asplund, M., & Sauval, A. J. 2007, Space Sci. Rev., 130, 105
Gustafsson, B., Edvardsson, B., Eriksson, K., et al. 2008, A&A, 486, 951
Jofre P., Heiter U., Soubiran C. et al. 2014, A&A, 564, A133
Johnson, C. I., & Pilachowski, C. A. 2010, ApJ, 722, 1373
King, I. 1962, AJ, 67, 471
Koo, J.-R., Kim, S.-L., Rey, S.-C., et al. 2007, PASP, 119, 1233
Kraft, R. P. 1979, ARA&A, 17, 309
Kraft, R. P. 1994, PASP, 106, 553
Kroupa, P. 2001, MNRAS, 322, 231
Lee, Y.-W., Joo, J.-M., Sohn, Y.-J., et al. 1999, Nature 402, 55
Lind, K., Primas, F., Charbonnel, C., Grundahl, F., & Asplund, M. 2009, A&A, 503, 545
Lind K., Asplund M., Barklem P. S., & Belyaev A. K. 2011, A&A, 528, A103
Lovis, C., Mayor, M. 2007, A&A, 472, 657
Magrini, L., Sestito, P., Randich, S., & Galli, D. 2009, A&A, 494, 95
Magrini, L., Randich, S., Zoccali, M., et al. 2010, A&A, 523, A11
Magrini, L., Randich, S., Romano, D., et al. 2014, A&A, 563, A44
Marino, A. F., Villanova, S., Piotto, G., et al. 2008, A&A, 490, 625
Marino, A. F., Sneden, C., Kraft, R. P., et al. 2011, A&A, 532, A8
Martell, S. L., Smolinski, J. P., Beers, T. C., & Grebel, E. K. 2011, A&A, 534, A136
Mathieu, R. D. 1984, ApJ, 284, 643
McNamara, B. J., & Sanders, W. L. 1977, A&A, 54, 569
Messina, S., Parihar, P., Koo, J.-R., et al. 2010, A&A, 513, A29
Milone, A. P., Piotto, G., Bedin, L. R., et al. 2012, ApJ, 744, 58
Miocchi, P. 2006, MNRAS, 366, 227
Piotto, G. 2009, IAU Symp., 258, 233
Randich, S., & Gilmore, G. 2013, The Messenger, 154, 47
Ramírez, S. V., & Cohen, J. G. 2002, AJ, 123, 3277
Robin, A. C., Reylé, C., Derrière, S., & Picaud, S. 2003, A&A, 409, 523
Sacco, G. G., Morbidelli, L., Franciosini, E., et al. 2014, A&A, 565, A113
Santos, Jr., J. F. C., Bica, E., & Dottori, H. 1990, PASP, 102, 454
Santos, Jr., J. F. C., Bonatto, C., & Bica, E. 2005, A&A, 442, 201
Schlegel D. J., Finkbeiner D. P., & Davis M., 1998, ApJ, 500, 525
Soubiran, C., & Girard, P. 2005, A&A, 438, 139
Spitzer L. Jr. 1969, ApJ, 158, L139
Stetson P. B. 1987, PASP, 99, 191
Sung, H., Bessell, M. S., Lee, H.-W., Kang, Y. H., & Lee, S.-W. 1999, MNRAS, 310, 982
Vallenari, A., Pasetto, S., Bertelli, G., et al. 2006, A&A, 451, 125
Vandame, B. 2002, in SPIE Conf. Ser. 4847, eds. J.-L. Starck, & F. D. Murtagh, 123
Ventura, P., D'Antona, F., Mazzitelli, I., & Gratton, R. 2001, ApJ, 550, L65
Villanova, S., Geisler, D., Carraro, G., Moni Bidin, C., & Munoz, C. 2013, ApJ, 778, 186
Walker, M. G., Mateo, M., Olszewski, E. W., et al. 2006, AJ, 131, 2114
Weidner, C., Kroupa, P., & Maschberger, T. 2009, MNRAS, 393, 663
Yuan H. B., Liu X. W., & Xiang M. S. 2013, MNRAS, 430, 2188
Zacharias, N., Finch, C. T., Girard, T. M., et al. 2012, VizieR Online Data Catalog: I/322

[1] Dipartimento di Fisica e Astronomia, Università di Padova, vicolo Osservatorio 3, 35122 Padova, Italy
e-mail: tristan.cantat@oapd.inaf.it
[2] INAF−Osservatorio Astronomico di Padova, vicolo Osservatorio 5, 35122 Padova, Italy
[3] INAF−Osservatorio Astronomico di Bologna, via Ranzani 1, 40127 Bologna, Italy
[4] School of Physics, Astronomy & Maths, University of Hertfordshire, Hatfield, Herts. AL10 9AB, UK
[5] Thueringer Landessternwarte, Sternwarte 5, 07778 Tautenburg, Germany
[6] CASU, Institute of Astronomy, Madingley Road, University of Cambridge, CB3 0HA, UK
[7] IGAM, Institute of Physics, University of Graz, Universitätsplatz. 5, 8010 Graz, Austria
[8] Departament d'Astronomia i Meteorologia, Universitat de Barcelona, Avda. Diagonal 647, 08028 Barcelona, Spain
[9] Royal Observatory of Belgium, Ringlaan 3, 1180 Brussel, Belgium
[10] Instituto de Astrofísica de Andalucía, CSIC, Apdo 3004, 18080 Granada, Spain
[11] European Southern Observatory, Karl-Schwarzschild-Str. 2, 85748 Garching bei München, Germany
[12] Department for Astrophysics, Nicolaus Copernicus Astronomical Center, ul. Rabiańska 8, 87-100 Toruń, Poland
[13] INAF−Osservatorio Astrofisico di Arcetri, Largo E. Fermi, 5, 50125 Firenze, Italy
[14] Dipartimento di Fisica e Astronomia, Università di Bologna, via Ranzani 1, 40127 Bologna, Italy
[15] Department of Astronomy, Indiana University, Bloomington, IN 47405, USA
[16] Massachusetts Institute of Technology and Kavli Institute for Astrophysics and Space Research, 77 Massachusetts Avenue, Cambridge, MA 02139, USA
[17] Institute of Theoretical Physics and Astronomy, Vilnius University, Goštauto 12, 01108 Vilnius, Lithuania
[18] INAF−Astrophysical Observatory of Torino, via Osservatorio 20, 10025 Pino Torinese, Italy
[19] Section of Astrophysics, Astronomy and Mechanics, Department of Physics, University of Athens, 15784 Athens, Greece
[20] INAF−Osservatorio Astrofisico di Catania, via S. Sofia 78, 95123 Catania, Italy
[21] Institute of Astronomy, University of Cambridge, Madingley Road, Cambridge CB3 0HA, UK
[22] Lund Observatory, Department of Astronomy and Theoretical Physics, Box 43, 221 00, Sweden
[23] INAF−Osservatorio Astronomico di Palermo, Piazza del Parlamento 1, 90134 Palermo, Italy
[24] Departamento de Astronomía, Universidad de Concepción, Casilla 160-C Concepción, Chile
[25] Laboratoire Lagrange (UMR7293), Université de Nice Sophia Antipolis, CNRS, Observatoire de la Côte d'Azur, BP 4229, 06304 Nice Cedex 4, France
[26] Spanish Virtual Observatory, Centro de Astrobiología (INTA-CSIC), PO Box 78, 28691 Villanueva de la Cañada, Madrid, Spain
[27] Millennium Institute of Astrophysics, Av. Vicuña Mackenna 4860, 782-0436 Macul, Santiago, Chile
[28] Pontificia Universidad Católica de Chile, Av. Vicuña Mackenna 4860, 782-0436 Macul, Santiago, Chile